OAK RIDGE
NATIONAL LABORATORY
MANAGED BY UT-BATTELLE
FOR THE DEPARTMENT OF ENERGY

ORNL/TM-2007/81

High Strain Rate Tensile Testing of DOP-26 Iridium

UT-BATTELLE
ORNL-27 (4-00)

November 2007

Prepared by
J. H. Schneibel, C. A. Carmichael, and E. P. George

ORNL/TM-2007/81

Radioisotope Power Systems Program

HIGH STRAIN RATE TENSILE TESTING OF DOP-26 IRIDIUM

J. H. Schneibel, C. A. Carmichael, and E. P. George

Date Published: November 2007

Prepared by
OAK RIDGE NATIONAL LABORATORY
Oak Ridge, Tennessee 37831-6283
managed by
UT-BATTELLE, LLC
for the
U.S. DEPARTMENT OF ENERGY
under contract DE-AC05-00OR22725

CONTENTS

Page

LIST OF FIGURES

LIST OF TABLES

HIGH STRAIN RATE TENSILE TESTING OF DOP-26 IRIDIUM*

J. H. Schneibel, C. A. Carmichael and E. P. George

ABSTRACT

The iridium alloy DOP-26 was developed through the Radioisotope Power Systems Program in the Office of Nuclear Energy of the Department of Energy. It is used for clad vent set cups containing radioactive fuel in radioisotope thermoelectric generator (RTG) heat sources which provide electric power for spacecraft. This report describes mechanical testing results for DOP-26. Specimens were given a vacuum recrystallization anneal of 1 hour at 1375°C and tested in tension in orientations parallel and perpendicular to the rolling direction of the sheet from which they were fabricated. The tests were performed at temperatures ranging from room temperature to 1090°C and strain rates ranging from 1×10^{-3} to 50 s^{-1}. Room temperature testing was performed in air, while testing at elevated temperatures was performed in a vacuum better than 1×10^{-4} Torr. The yield stress (YS) and the ultimate tensile stress (UTS) decreased with increasing temperature and increased with increasing strain rate. Between 600 and 1090°C, the ductility showed a slight increase with increasing temperature. Within the scatter of the data, the ductility did not depend on the strain rate. The reduction in area (RA), on the other hand, decreased with increasing strain rate. The YS and UTS values did not differ significantly for the longitudinal and transverse specimens. The ductility and RA values of the transverse specimens were marginally lower than those of the longitudinal specimens.

INTRODUCTION

Iridium exhibits a unique combination of a high melting point (2443°C), good oxidation resistance, and excellent high-temperature strength [1]. In a review of 25 years of research on iridium as a structural material, George and Liu [1] showed that its mechanical properties can be significantly improved by macroalloying (typically >1 wt%) and microalloying (typically <1 wt%). Macroalloying with W or Hf increases the yield strength and the recrystallization temperature [1-6]. Microalloying with Th raises the recrystallization temperature, impedes grain growth, and increases the tensile impact ductility by strengthening the grain boundaries [1,2-5]. The beneficial effect of Th is due to grain boundary segregation [7] and the formation of fine Ir_5Th precipitates [8]. The Th may be partially substituted with Ce without any loss in the mechanical properties [9,10]. In fact, newly developed alloys containing Th and Ce exhibit improved high-temperature impact ductility and weldability [1].

*Research sponsored by the Office of Radioisotope Power Systems at the Oak Ridge National Laboratory, managed by UT-Battelle, LLC for the U.S. Department of Energy under contract number DE-AC05-00OR22725

Iridium exhibits the face-centered cubic crystal structure. Unlike other elements with this crystal structure, its mechanical properties are strain rate sensitive. The mechanical behavior of iridium thus resembles that of body-centered cubic metals [1]. As a result of the strain rate sensitivity, the ductility of iridium decreases with increasing strain rate. For example, whereas the elongation to fracture at a temperature of 800°C and a strain rate of $\sim 10^{-3}$ s^{-1} reaches ~55%, an increase in the strain rate by six orders of magnitude to $\sim 10^{3}$ s^{-1} reduces this value to ~15% [10]. In critical applications of iridium it is therefore important to characterize the strain rate dependence of the mechanical properties.

An important application of iridium is radioisotope thermoelectric generators (RTGs) for space power applications [11]. In RTGs, the iridium alloy DOP-26 is used as cladding for $^{238}PuO_2$ fuel. DOP-26 was developed at the Oak Ridge National Laboratory [1-5]. It is an Ir-0.3 wt% W alloy containing 60 wppm Th to improve the high temperature impact ductility. To date, most of the mechanical property testing of DOP-26 consisted of tensile tests at $\sim 10^{-3}$ s^{-1} and impact tests at $\sim 10^{3}$ s^{-1}. In order to add intermediate strain rates to this mechanical properties database, the present work measures the strength and ductility of DOP-26 at temperatures ranging from room temperature to 1090°C and strain rates ranging from 10^{-3} s^{-1} to 50 s^{-1}. Tests were performed parallel and perpendicular to the sheet rolling direction in order to assess the effect of the orientation on the mechanical properties.

EXPERIMENTAL PROCEDURE

SPECIMEN PREPARATION

Tensile specimens were electro-discharge machined from stress-relieved DOP-26 iridium sheet with a thickness between 0.6 and 0.7 mm, followed by grinding to the final dimensions (Fig. 1). The edges of the gage lengths and fillet radii of the specimens were polished with 320 and 600 grit SiC paper. After dimensional inspection, the specimens were cleaned for 30 minutes in a solution of 3 parts HCl and 1 part HNO_3 by volume, plus 15 vol% HF (conc.), followed by rinsing in distilled water and ethanol. The cleaned specimens were annealed for 1 hour at 1375°C in a vacuum better than 1×10^{-4} Torr. The gage length of each specimen was marked with a row of seven 1000-g microhardnesss impressions spaced at 1.5-mm intervals.

MECHANICAL TESTING

The tensile tests were carried out in a servohydraulic 1321 Instron testing machine equipped with a turbo-pumped vacuum system and a radio frequency (RF) heater for heating up a tantalum susceptor supported by an alumina tube. Prior to testing, each specimen was inserted into mating molybdenum alloy (TZM) grips that supported it on the 5 mm radius shoulders. Room temperature tests were performed in air. Tests above room temperature were performed in a vacuum better than 1×10^{-4} Torr. The specimen temperature was measured with two Pt-Pt/Rh type S thermocouples that were placed on the specimen gage section and wrapped with 0.4 mm diameter Pt wire. The distance between the two thermocouples was typically 5 mm.

During testing, the temperature was held within ±10°C of the target value. The load cell was calibrated with an accuracy of ±1% of its reading. The cross-sectional area of the specimens was determined from the specimen thickness and the width W2 (Fig. 1) with an accuracy of 1%, resulting in an overall accuracy of the stress measurement of ±2%.

Because of the small size of the specimens, the load signal obtained at low strain rates (1×10^{-3} s^{-1}) exhibited noise and was therefore smoothed. In a few of the slow tests at high temperatures, the reading of the load cell at zero load drifted during the test. If the drift corresponded to more than about 10 MPa at the completion of the test, the stress data were adjusted by assuming that the reading of the load cell at zero load drifted linearly with time.

For the tests carried out at 10^{-3} and 10 s^{-1}, an elastic load-displacement line (which was governed by the compliances of the testing system and the specimen) was obtained by fitting a straight line to the region of maximum slope below the yield point (Fig. 2). It should be pointed out that this ***elastic line*** was not truly elastic – upon loading, plastic seating of the specimens occurred, presumably due to an imperfect mating between the specimen shoulders and the grips. This resulted in specimen-to-specimen variations in the slope of the "elastic" line by up to a factor of 2. The curve ID#43 in Fig. 3 provides an example of this effect: this specimen was preloaded to approximately 50 MPa, unloaded, and then tested. It is readily seen that the elastic slope below 50 MPa is higher than that above 50 MPa. Presumably, the reason for this is the elimination of any plastic deformation below 50 MPa because of the preloading. In the following, we will use the term "elastic line" even though, strictly speaking, it is not an elastic line. At a strain rate of 50 s^{-1}, the elastic load-displacement line could not be determined since the data acquisition rate was limited to 5 kHz corresponding to a point-to-point spacing of 1% strain. Therefore, an average value of the elastic line obtained from the 10^{-3} and 10 s^{-1} data was used instead. At 50 s^{-1} no attempt was made to determine the yield stress.

At 10 and 50 s^{-1}, oscillations of the stress were usually observed during testing. These oscillations ("ringing") were associated with the load frame and the upper load train which was attached to the load cell. Their amplitude was significantly reduced by reducing the mass of the upper load train from an initial value of 750 g to approximately 300 g. However, the ringing could not be entirely eliminated. At 10 s^{-1}, approximately 5 oscillations were observed during tests performed at 600°C and above. Stress averaging was carried out near the maximum stress in order to determine the ultimate tensile stress (UTS) more precisely. At 50 s^{-1}, the tests took place in less than one ringing period. This resulted in differences in the shape of the stress-strain curves for nominally identical testing conditions, resulting in additional scatter.

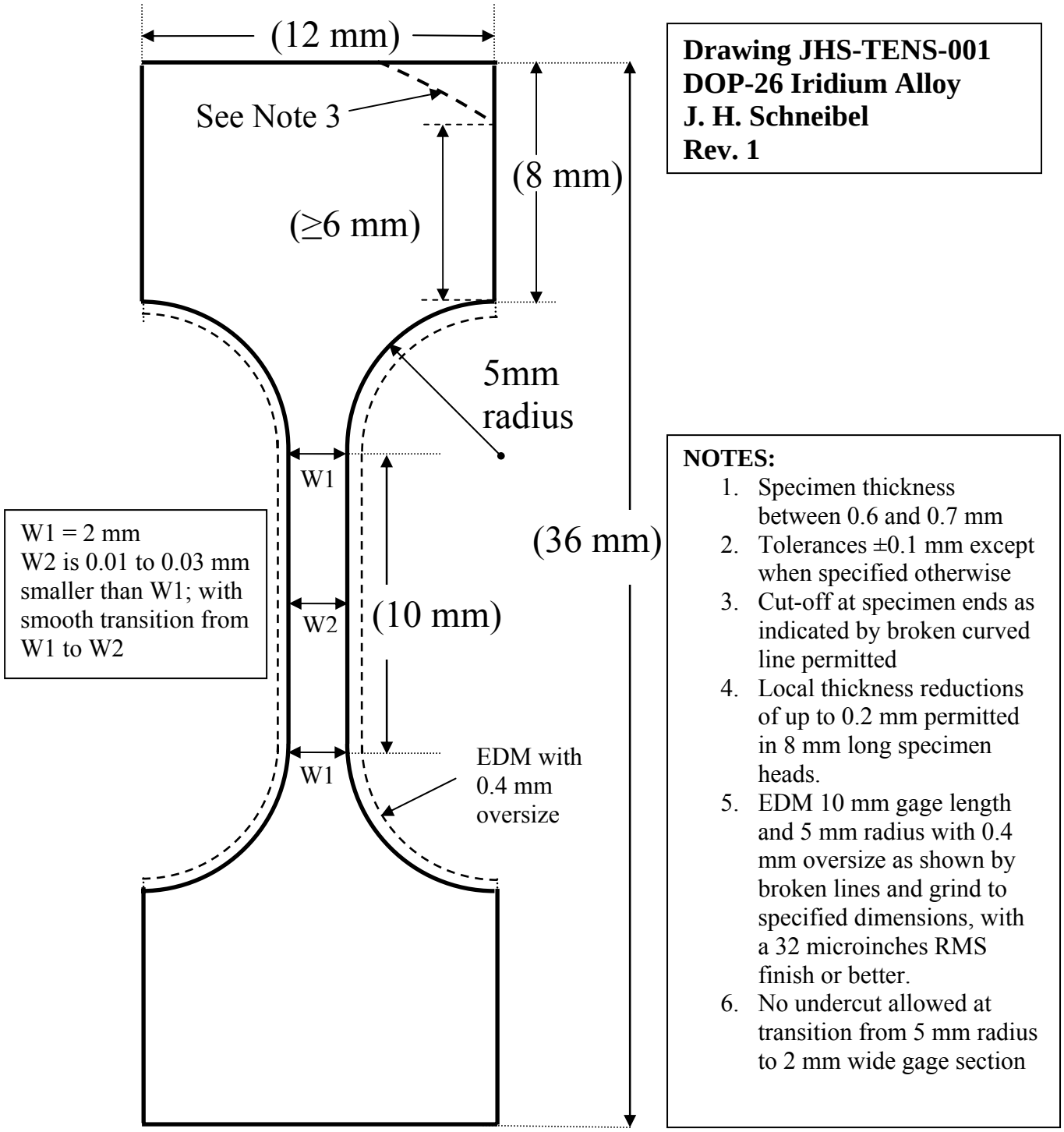

Inspection points for Quality Control:

1. Specimen width W1 (top), W1 (bottom), and W2
2. Specimen thickness in center of gage length
3. Verification of the 5 mm radii for the four shoulders

Fig. 1. Machining instructions for tensile test specimens.

STRAIN EVALUATION

The low yield stress and small size of the specimens precluded the attachment of extensometers to the specimen gage. Realistic stress-strain curves were therefore obtained from the load vs. crosshead extension by a correction procedure based on the spacing of the microhardness indents after testing. First, uncorrected specimen strains, i.e., ***"crosshead strains,"*** were obtained by dividing the crosshead extension by the nominal gage length, 10 mm. An elastic line was drawn through the maximum slope portion of the test curve below the yield point, and a line with the same slope through the point of fracture as shown in Fig. 2. The ***"crosshead fracture strain"*** was defined as the horizontal separation between those two lines. The ***"crosshead plastic strain"*** for each point on the test curve in Fig. 2 was defined as the horizontal distance between the elastic line and that point. In the case of sudden fracture at the UTS, the elastic line at fracture was placed through the point at which the UTS was observed. In the case of gradual fracture, the elastic line was placed through a point on the decreasing part of the stress-strain curve corresponding to 0.8 times the UTS. The experimental variations in the slope of the elastic lines resulted in an uncertainty in the crosshead fracture strains on the order of ±1% strain, but in some cases an uncertainty of up to ±2% strain was encountered.

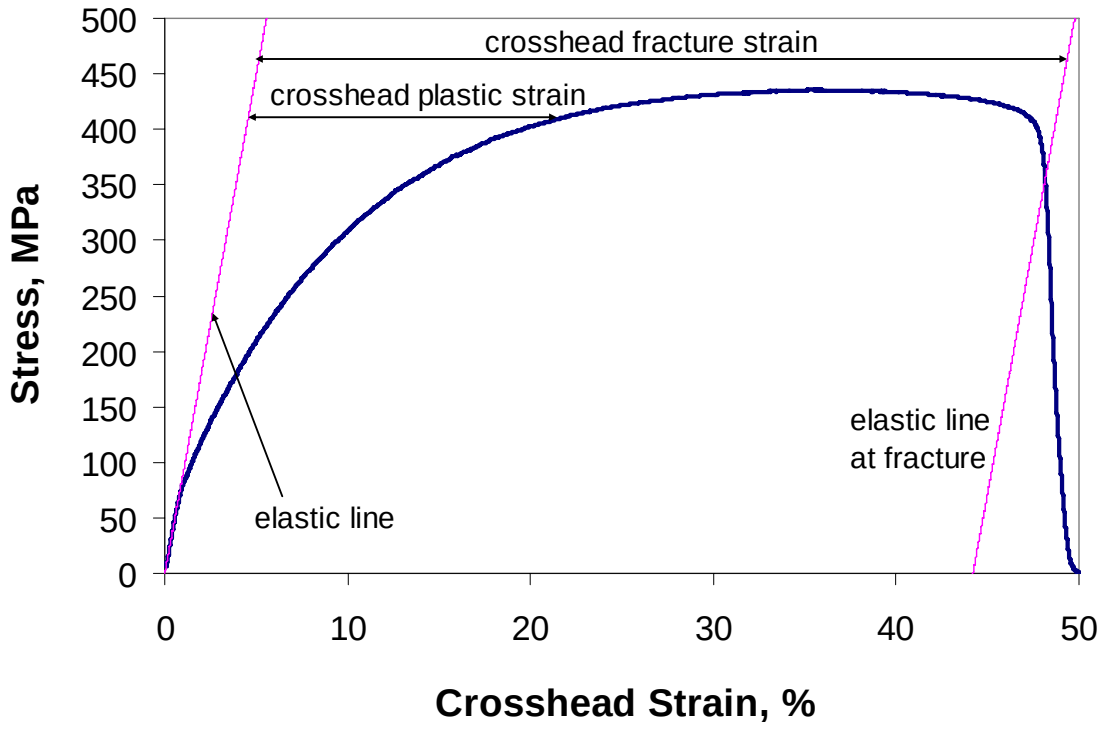

Fig. 2. Stress vs. crosshead strain.

Deformation of the specimens did not occur exclusively in the 10 mm gage length. During testing the deformation propagated to the specimen shoulders. This resulted in errors in the crosshead fracture strain (which was calculated assuming a 10 mm gage length). In order to

obtain a realistic measure of the specimen plastic strain, corrections using the "***indent fracture strain***" were made. The indent fracture strain is the average of the local strains calculated from the increase in the indent-indent spacing after testing a specimen. The strain corresponding to the two indents between which fracture occurred was not evaluated, i.e., only 5 spacings were typically evaluated. Occasionally, an indent could not be found after testing, and then only 4 spacings were available for the evaluation of the fracture strain.

The indent fracture strain was not used directly to correct the crosshead plastic strain. This is because the scatter in the indent fracture strains was significantly higher than that in the crosshead fracture strains. The following procedure was adopted to calculate the specimen plastic strain (Fig. 2): For each specimen, the ratio of the indent fracture strain and the crosshead fracture strain was evaluated. For each test temperature, the average of these ratios was calculated. The ***"specimen plastic strain"*** was calculated by multiplying the crosshead plastic strain with the strain correction factor pertaining to the test temperature. The final plots of (engineering) stress vs. (engineering) strain were obtained from curves of the stress vs. the crosshead strain such as that in Fig. 2 by replacing the crosshead plastic strain with the specimen plastic strain. The ***fracture strains*** (also called ***ductility*** or ***elongation to fracture***) were obtained by multiplying the crosshead fracture strains with the corresponding strain correction factors.

EVALUATION OF REDUCTION IN AREA

The reduction in area (RA) was determined from the initial cross section, A_i, and the fracture area, A_f, of the tested specimens using the relationship:

$$RA = 100\% \times (A_i - A_f)/A_i$$

A_i was obtained by multiplying the specimen thickness with the specimen width W2 (Fig. 2). The projected fracture surface area A_f of each specimen was evaluated from scanning electron microscope micrographs using a 500 lines per inch calibration standard. A_f could be determined with an accuracy of 3%. Only one of the two fracture surfaces of each specimen was examined.

RESULTS AND DISCUSSION

STRESS-STRAIN CURVES

Tables I and II tabulate the slopes of the elastic lines, the crosshead fracture strains, and the indent fracture strains for the longitudinal and transverse tests. The ratios of the crosshead and indent fracture strains were averaged to determine the strain correction factor for each temperature (see Table III). Table III shows that the strain correction factor for room temperature is much smaller than the corresponding values at 600°C and above. The reason for this is the extremely high work hardening capacity of DOP-26 at room temperature – the pronounced hardening of the gage section during testing causes significant plastic deformation

in the shoulder and head sections of the specimen, and a concomitant increase in the effective gage length.

The fracture strains were determined by multiplying the crosshead fracture strains with the corresponding correction factor (Table III). The crosshead plastic strains were multiplied with the appropriate correction factor to obtain the final stress-strain curves. These curves are plotted in Figs. 3-23.

Table I. Fracture strains and slopes of elastic lines for longitudinal DOP-26 specimens

ID#	Strain rate, s^{-1}	T, °C	Slope of elastic line, MPa/% crosshead strain	Crosshead fracture strain, %	Indent fracture strain, %
1	1×10^{-3}	25	217	14.3	8.6
32	1×10^{-3}	25	183	14.4	9.0
43	1×10^{-3}	25	202	16.9	10.0
2	1×10^{-3}	600	90	44.2	34.7
19	1×10^{-3}	600	248	38.8	25.8
33	1×10^{-3}	600	112	41.1	28.5
20	1×10^{-3}	750	87	45.0	30.8
35	1×10^{-3}	750	110	43.6	32.4
4	1×10^{-3}	900	97	47.6	33.5
21	1×10^{-3}	900	113	47.2	34.8
36	1×10^{-3}	900	92	49.8	38.8
5	1×10^{-3}	1090	227	54.0	39.1
37	1×10^{-3}	1090	147	52.7	38.2
45	1×10^{-3}	1090	90	52.6	40.8
6	10	25	148	15.7	10.1
23	10	25	204	16.2	9.4
38	10	25	168	18.4	11.4
7	10	600	99	41.8	33.1
24	10	600	116	43.6	32.5
39	10	600	216	45.3	34.6
8	10	750	108	46.9	38.3
25	10	750	182	40.7	27.3
40	10	750	142	45.9	35.8
9	10	900	102	42.2	30.5
26	10	900	146	33.7	25.7
41	10	900	171	42.2	32.2
11	10	1090	177	50.0	35.4
27	10	1090	215	49.9	40.1
42	10	1090	118	45.7	35.5
12	50	25	150	15.5	9.5
28	50	25	150	15.9	10.3
44	50	25	150	14.3	9.4
13	50	600	150	46.0	33.4
29	50	600	150	47.3	33.1
50	50	600	150	44.9	34.5
14	50	750	150	52.5	38.2
30	50	750	150	49.2	34.4
48	50	750	150	49.6	38.6
15	50	900	150	44.5	30.5
17	50	900	150	43.6	32.1
47	50	900	150	44.5	33.6
16	50	1090	150	60.0	46.1
46	50	1090	150	47.9	34.8
49	50	1090	150	46.8	31.1

Table II. Fracture strains and slopes of elastic lines for transverse DOP-26 specimens

ID#	Strain rate, s^{-1}	T, °C	Slope of elastic line, MPa/% crosshead strain	Crosshead fracture strain, %	Indent fracture strain, %
51T	1×10^{-3}	750	92	43.3	33.4
52T	1×10^{-3}	750	155	40.0	29.5
66T	1×10^{-3}	750	145	40.0	27.3
53T	1×10^{-3}	1090	152	46.1	36.3
54T	1×10^{-3}	1090	107	45.7	30.1
68T	1×10^{-3}	1090	91	46.7	35.5
55T	10	750	176	42.8	31.2
62T	10	750	141	43.6	36.0
64T	10	750	142	45.9	33.8
58T	10	1090	196	46.6	38.3
65T	10	1090	101	38.9	27.4
67T	10	1090	133	47.0	38.6
56T	50	750	150	45.7	35.5
59T	50	750	150	46.8	38.1
61T	50	750	150	42.7	33.4
57T	50	1090	150	52.1	41.1
60T	50	1090	150	46.1	34.4
63T	50	1090	150	49.7	39.7

Table III. Strain correction factors for calculating the plastic strain from curves of stress vs. crosshead strain

T, °C	Strain correction factor, longitudinal specimens	Strain correction factor, transverse specimens
25	0.620	
600	0.738	
750	0.737	0.763
900	0.738	
1090	0.741	0.767

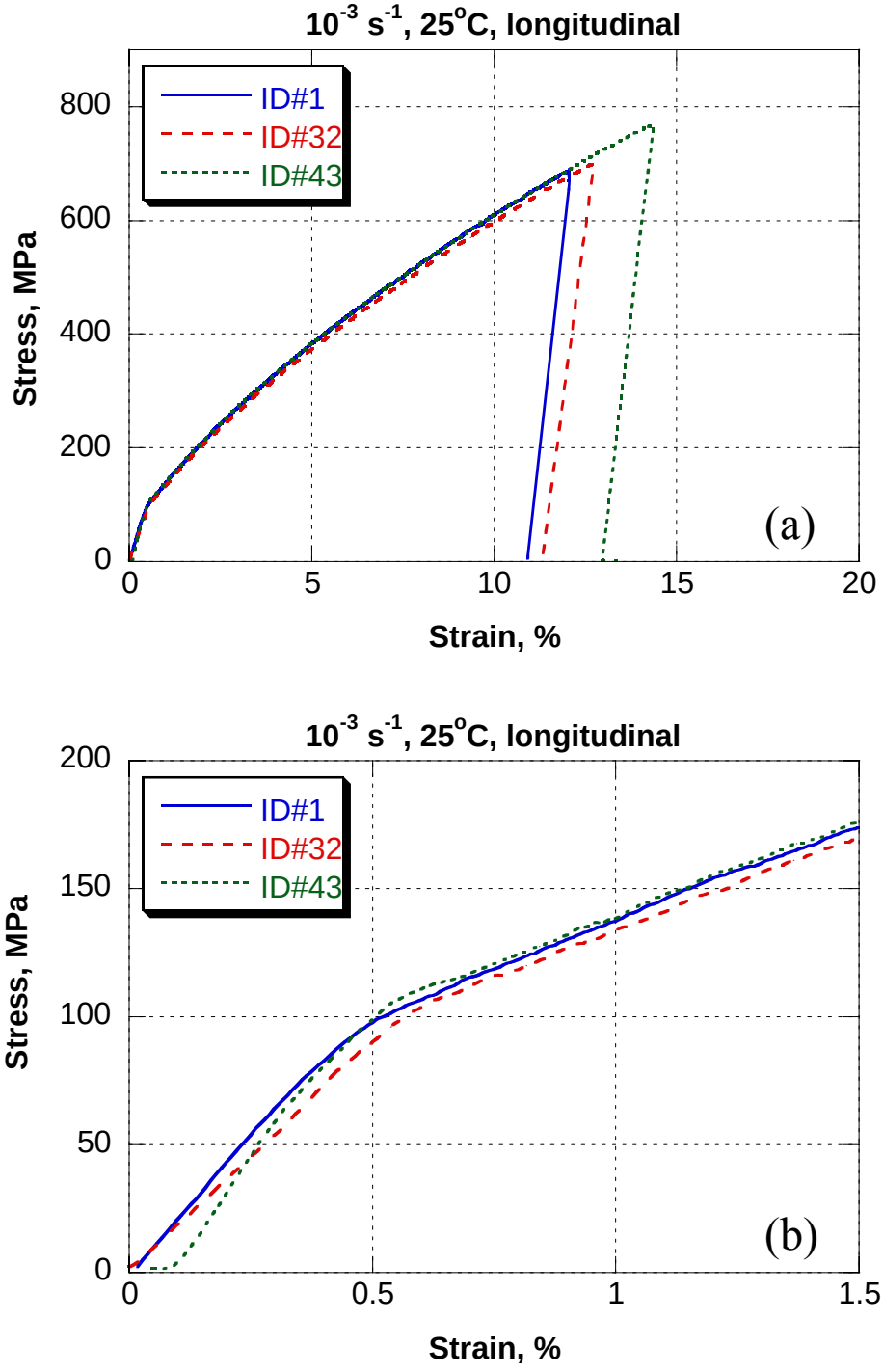

Fig. 3. Stress-strain curves at 10^{-3} s^{-1} and 25°C, longitudinal specimen orientation, (a) full curves, (b) yield region.

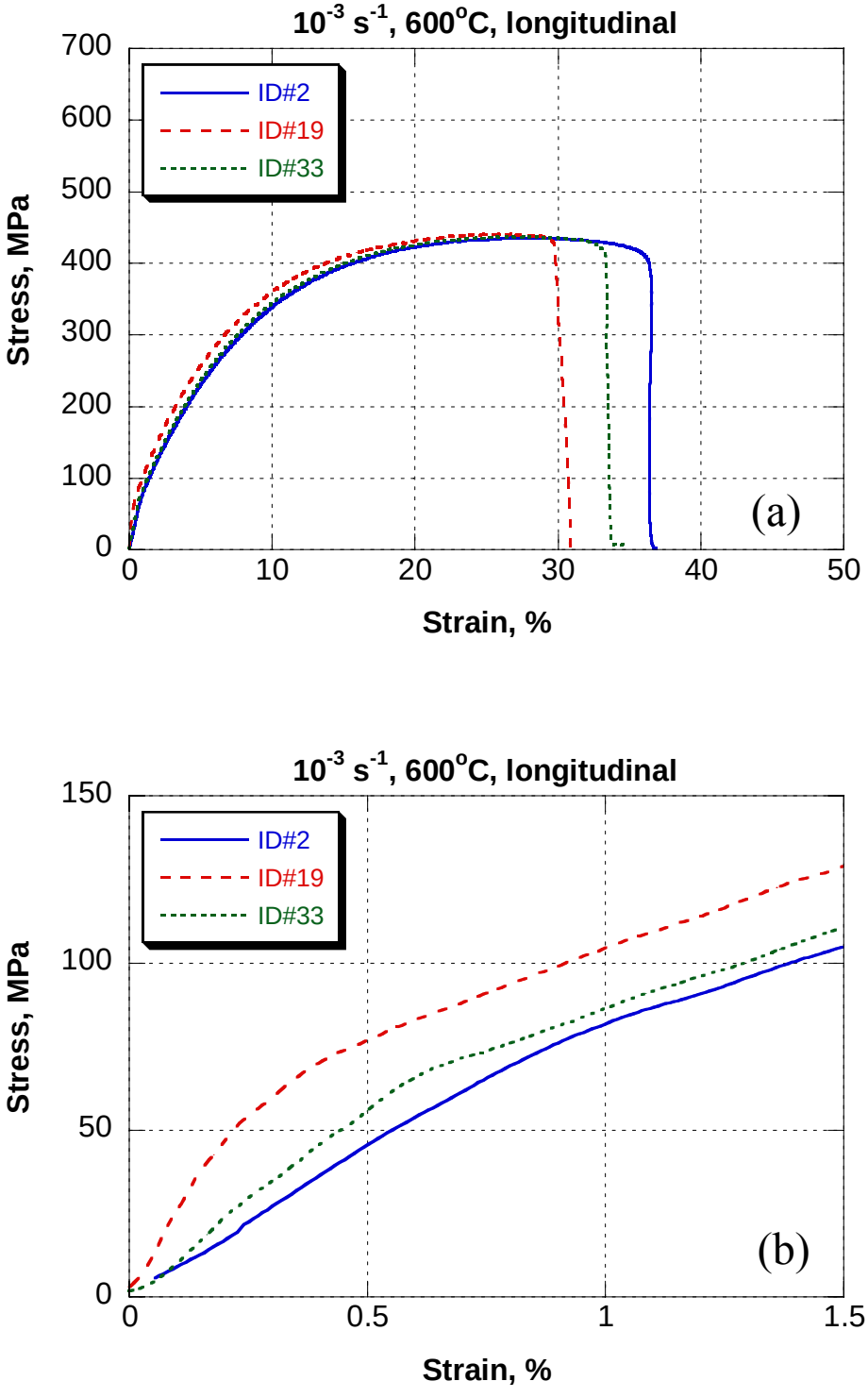

Fig. 4. Stress-strain curves at 10^{-3} s^{-1} and 600°C, longitudinal specimen orientation, (a) full curves, (b) yield region.

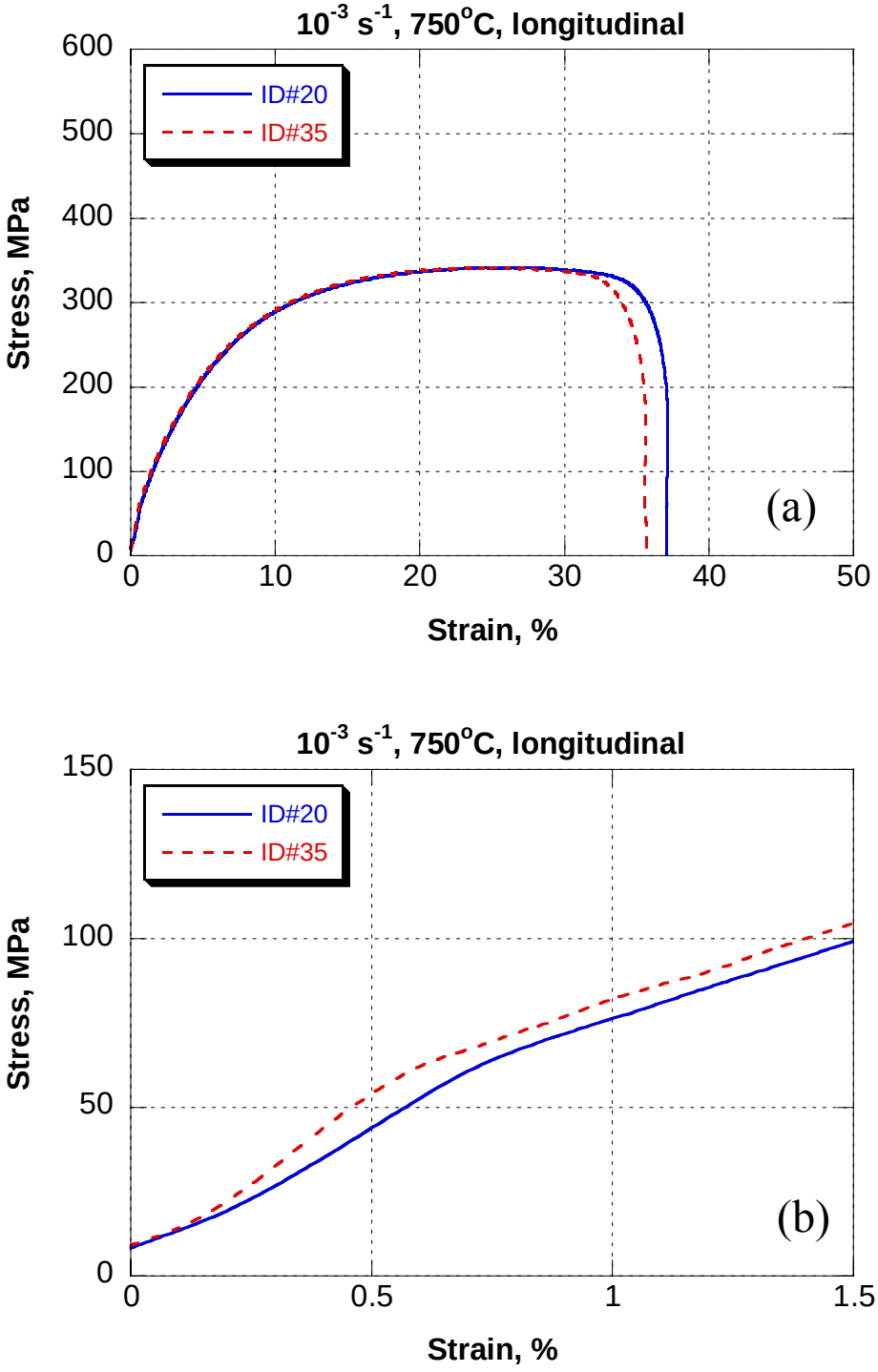

Fig. 5. Stress-strain curves at 10^{-3} s^{-1} and 750°C, longitudinal specimen orientation, (a) full curves, (b) yield region.

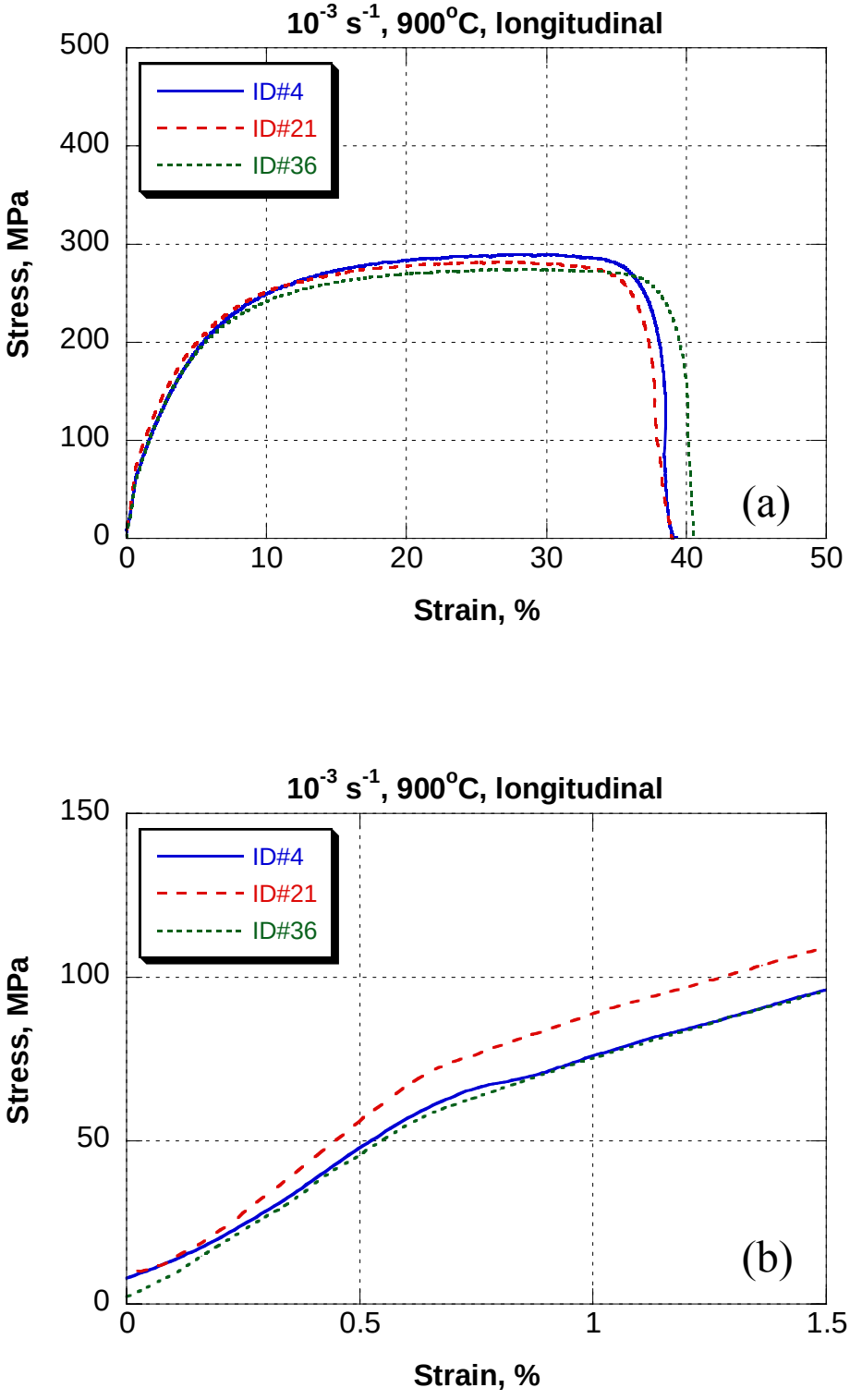

Fig. 6. Stress-strain curves at 10^{-3} s^{-1} and 900°C, longitudinal specimen orientation, (a) full curves, (b) yield region.

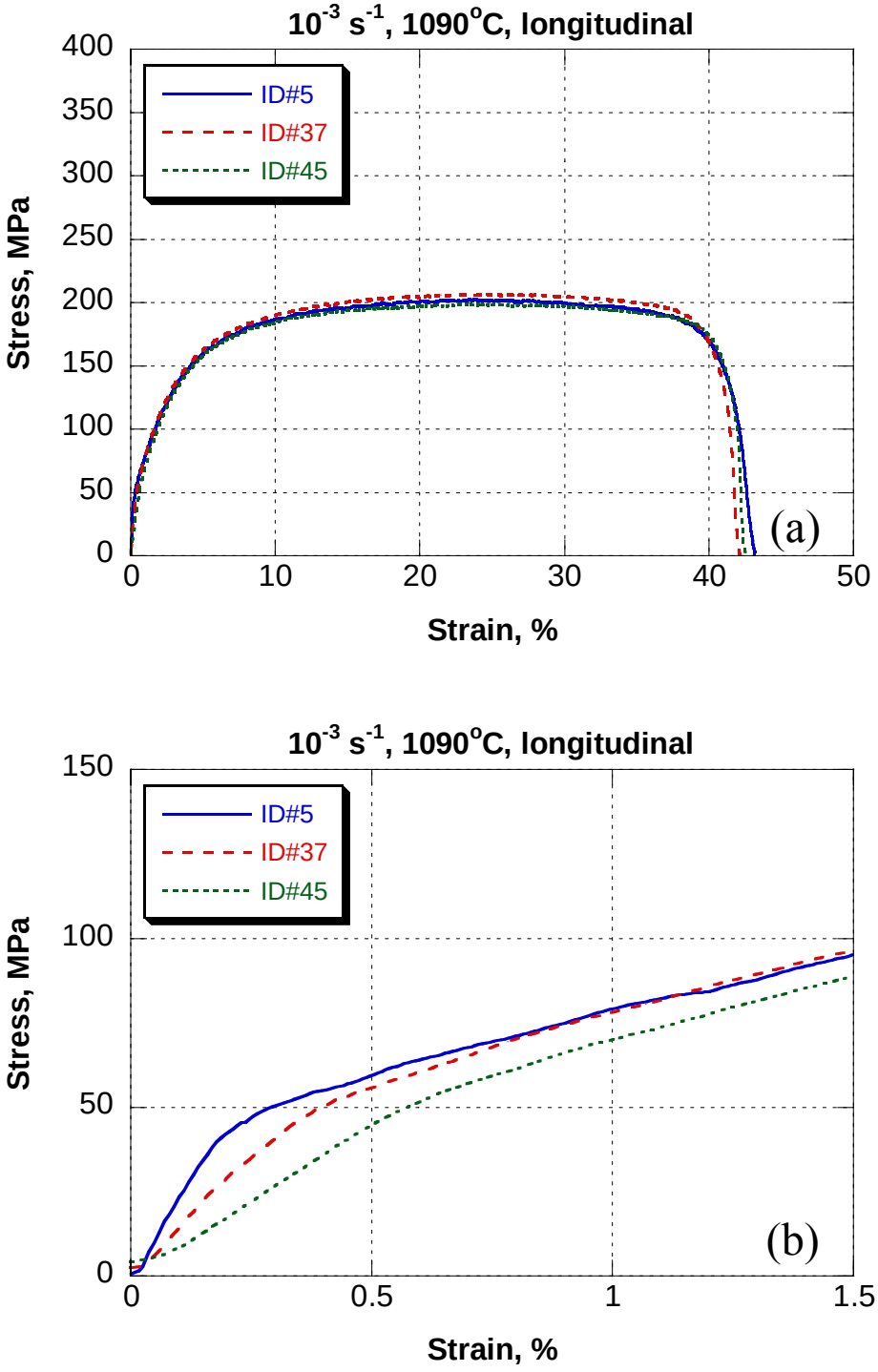

Fig. 7. Stress-strain curves at 10^{-3} s^{-1} and 1090°C, longitudinal specimen orientation, (a) full curves, (b) yield region.

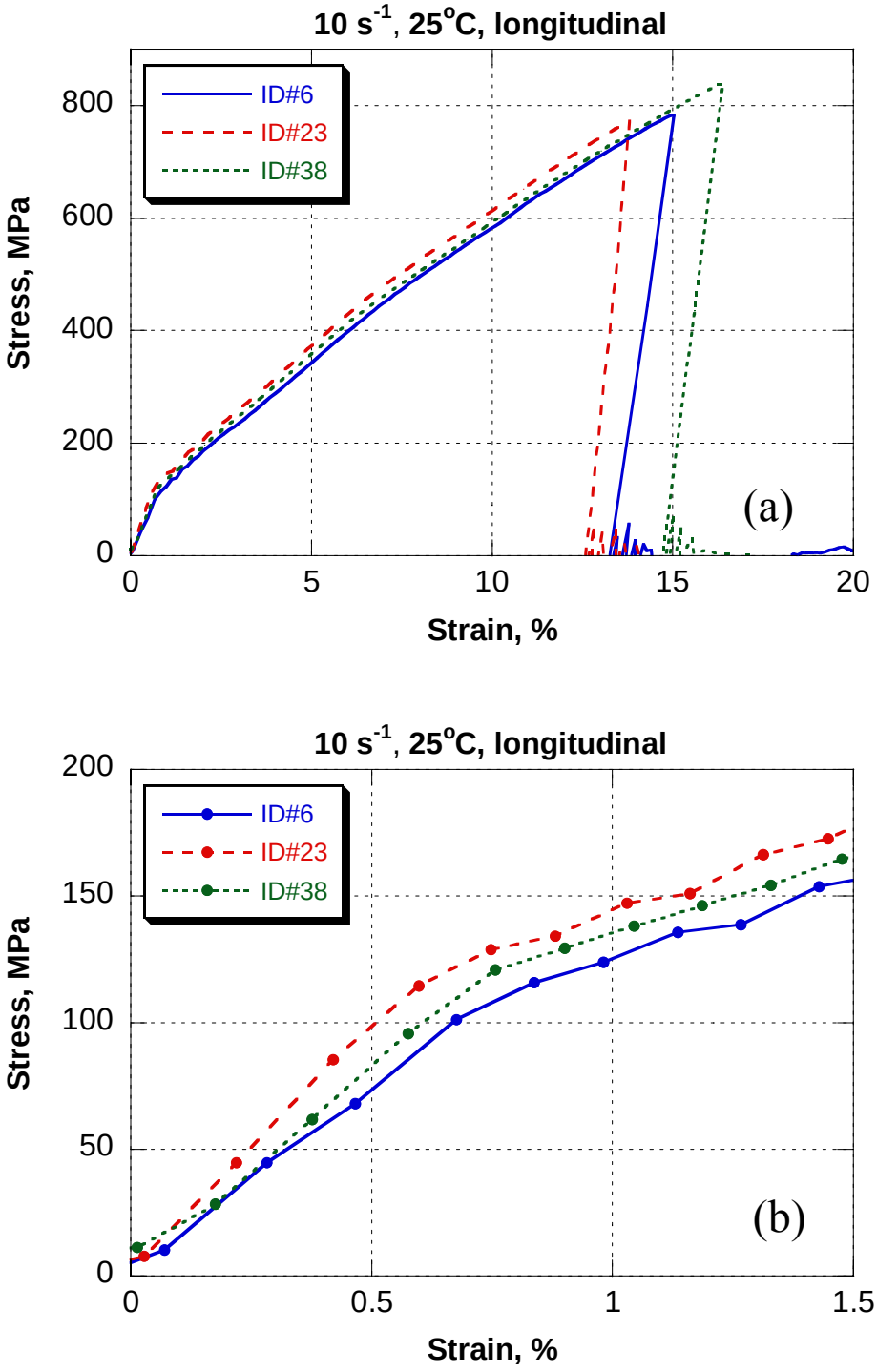

Fig. 8. Stress-strain curves at 10 s^{-1} and 25°C, longitudinal specimen orientation, (a) full curves, (b) yield region.

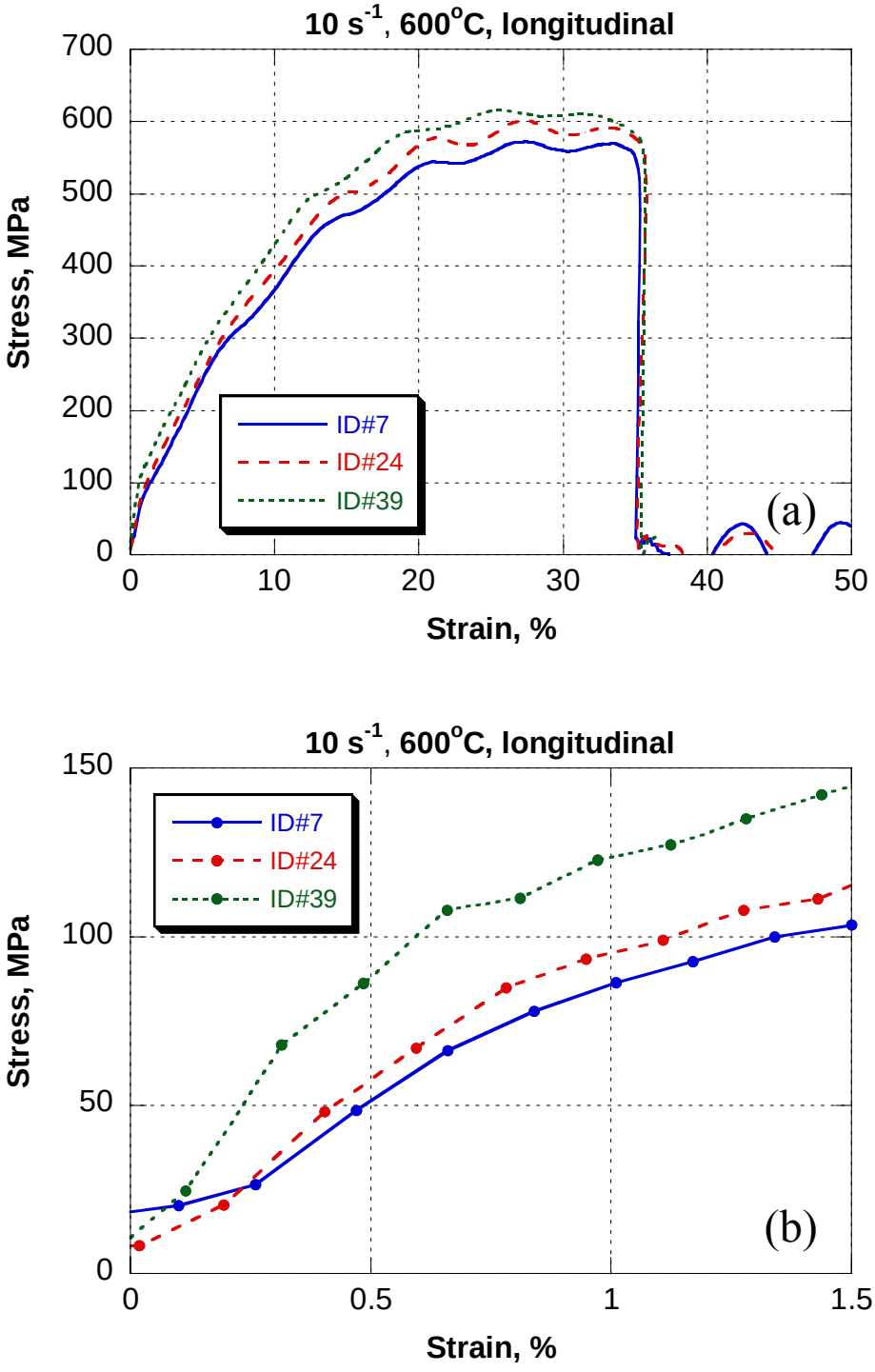

Fig. 9. Stress-strain curves at 10 s^{-1} and 600°C, longitudinal specimen orientation, (a) full curves, (b) yield region.

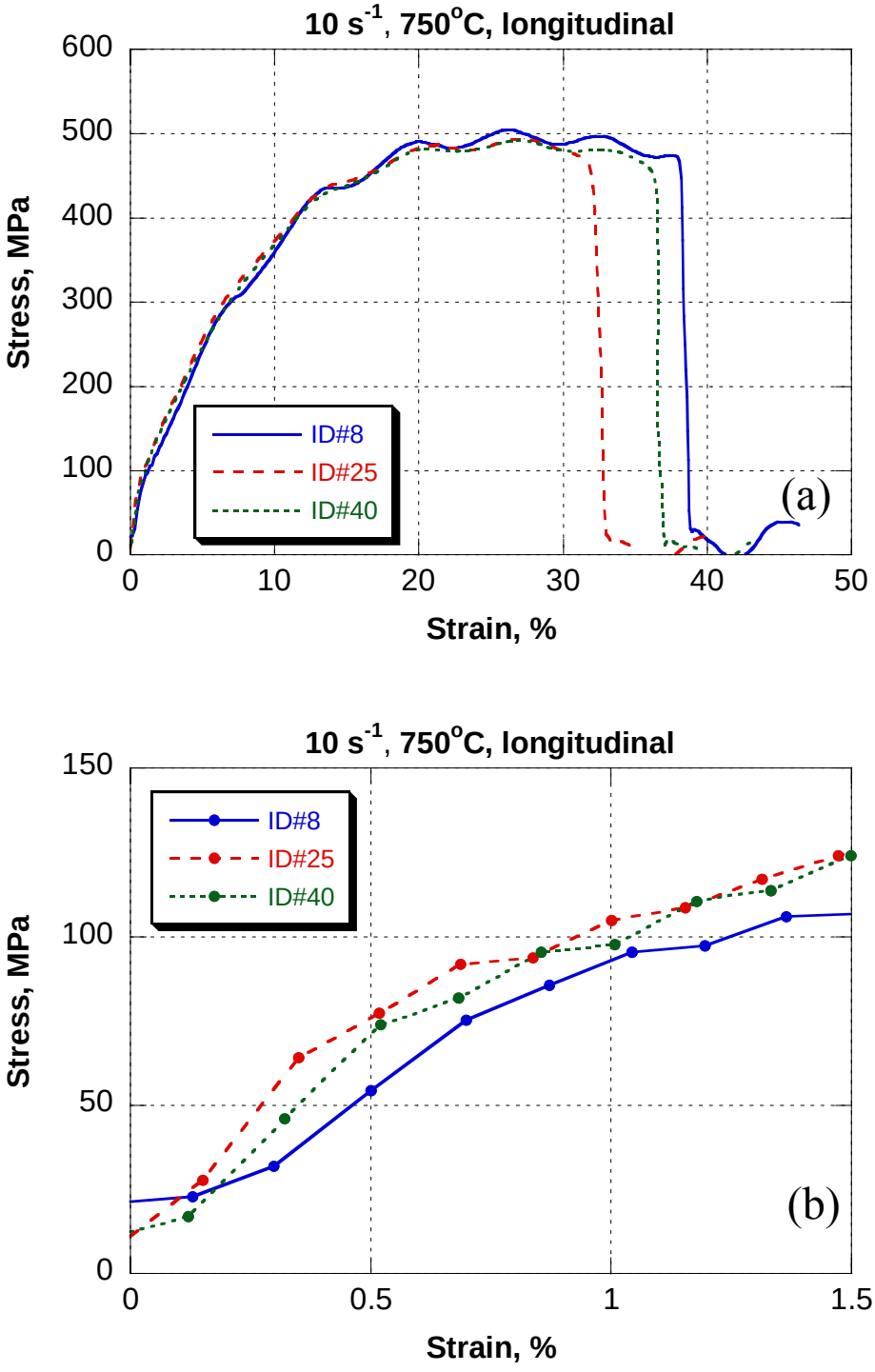

Fig. 10. Stress-strain curves at 10 s^{-1} and 750°C, longitudinal specimen orientation, (a) full curves, (b) yield region.

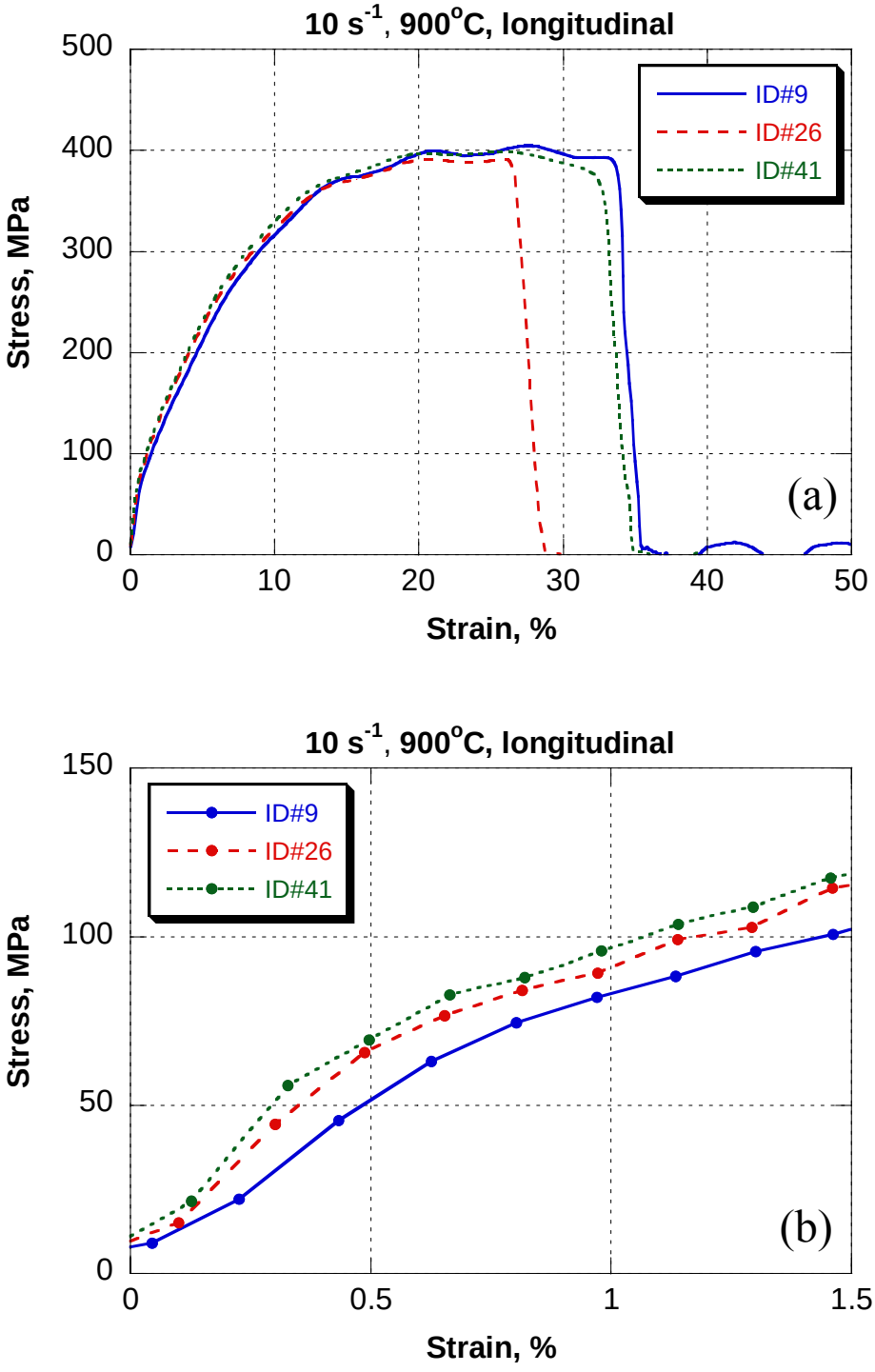

Fig. 11. Stress-strain curves at 10 s^{-1} and 900°C, longitudinal specimen orientation, (a) full curves, (b) yield region.

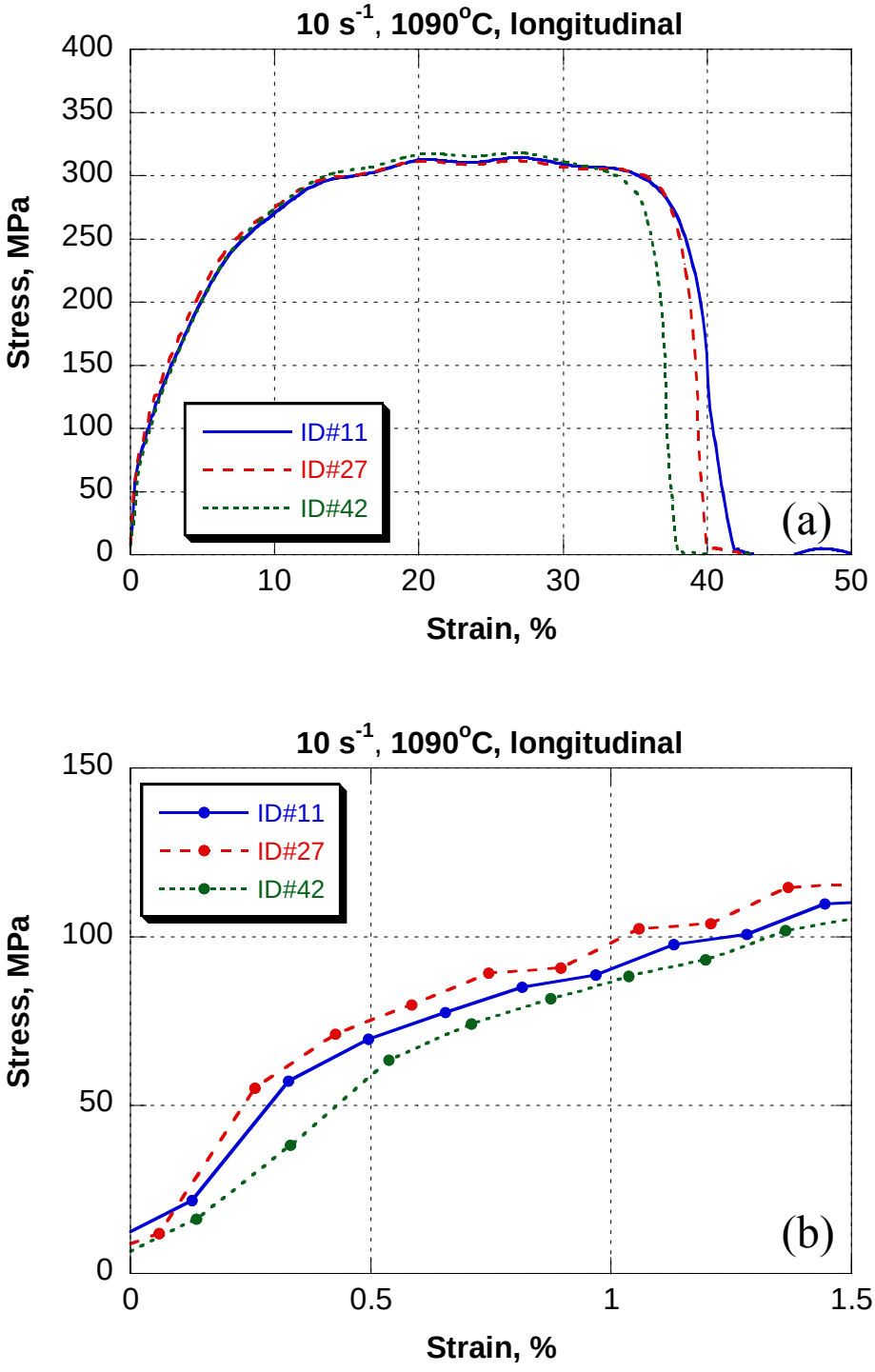

Fig. 12. Stress-strain curves at 10 s^{-1} and 1090°C, longitudinal specimen orientation, (a) full curves, (b) yield region.

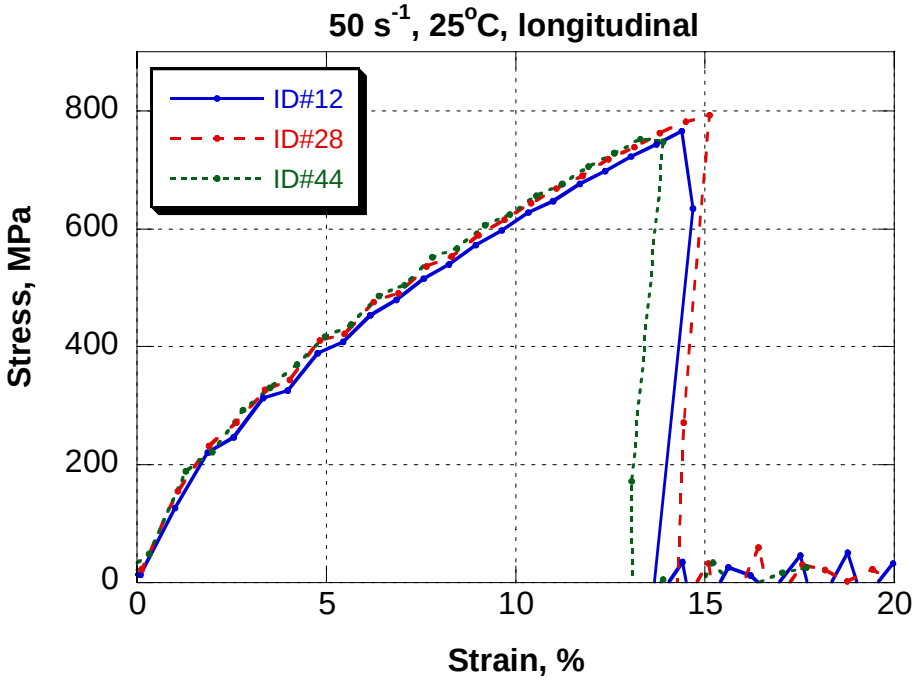

Fig. 13. Stress-strain curves at 50 s^{-1} and 25°C, longitudinal specimen orientation.

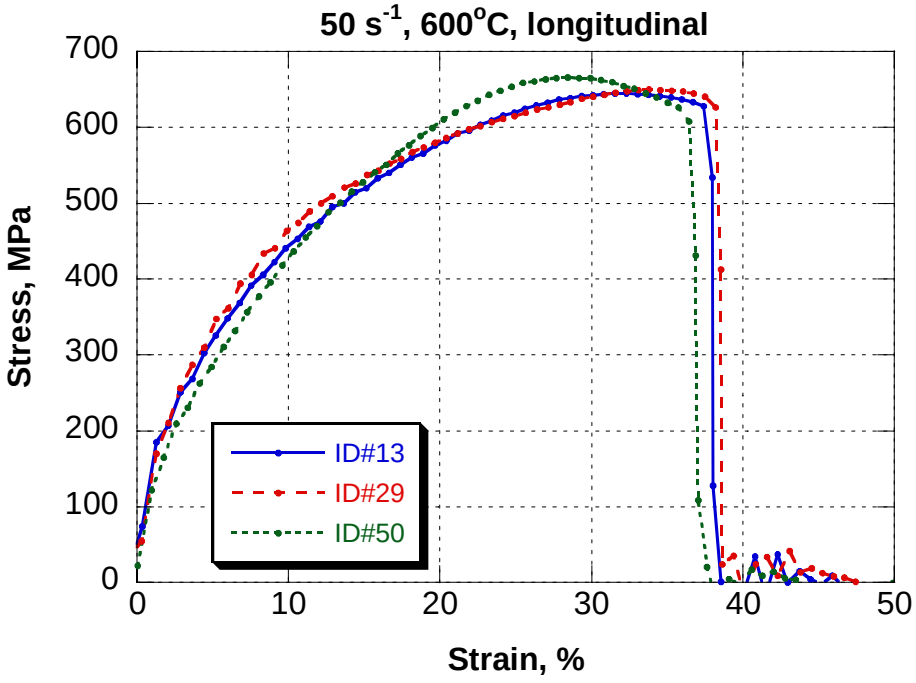

Fig. 14. Stress-strain curves at 50 s^{-1} and 600°C, longitudinal specimen orientation.

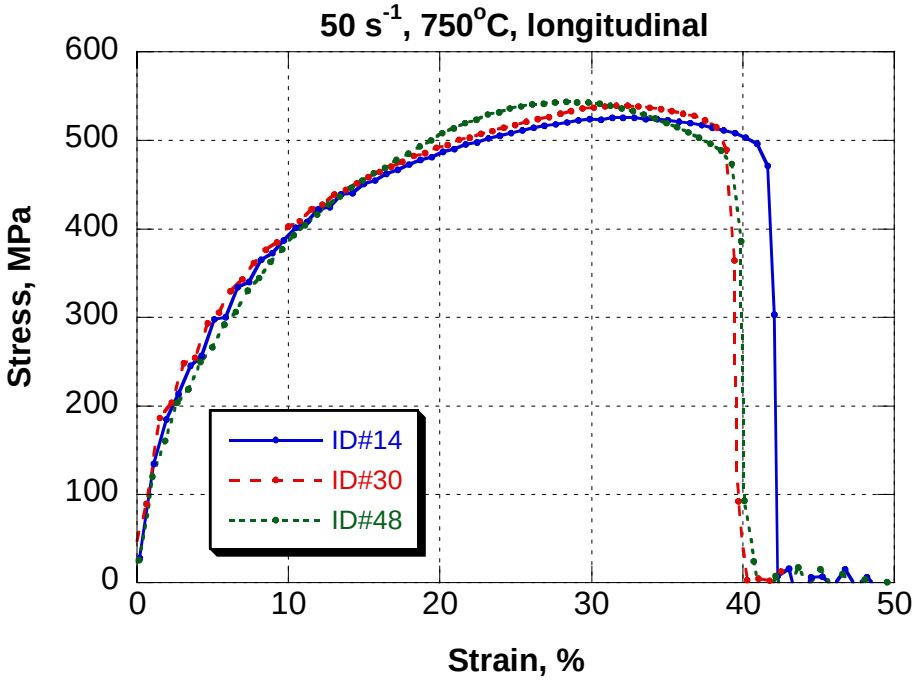

Fig. 15. Stress-strain curves at 50 s^{-1} and 750°C, longitudinal specimen orientation.

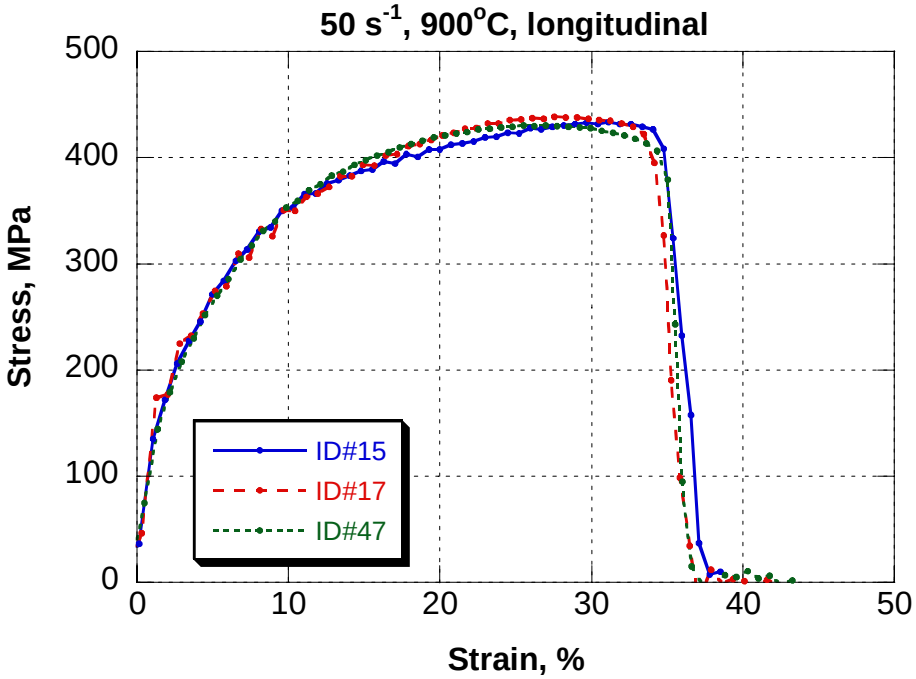

Fig. 16. Stress-strain curves at 50 s^{-1} and 900°C, longitudinal specimen orientation.

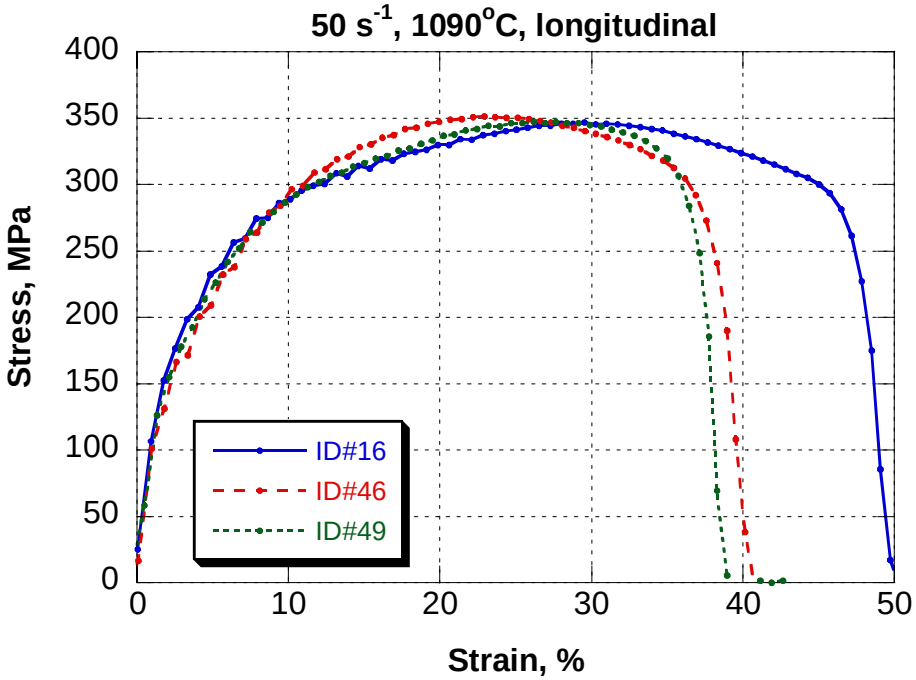

Fig. 17. Stress-strain curves at 50 s^{-1} and 1090°C, longitudinal specimen orientation.

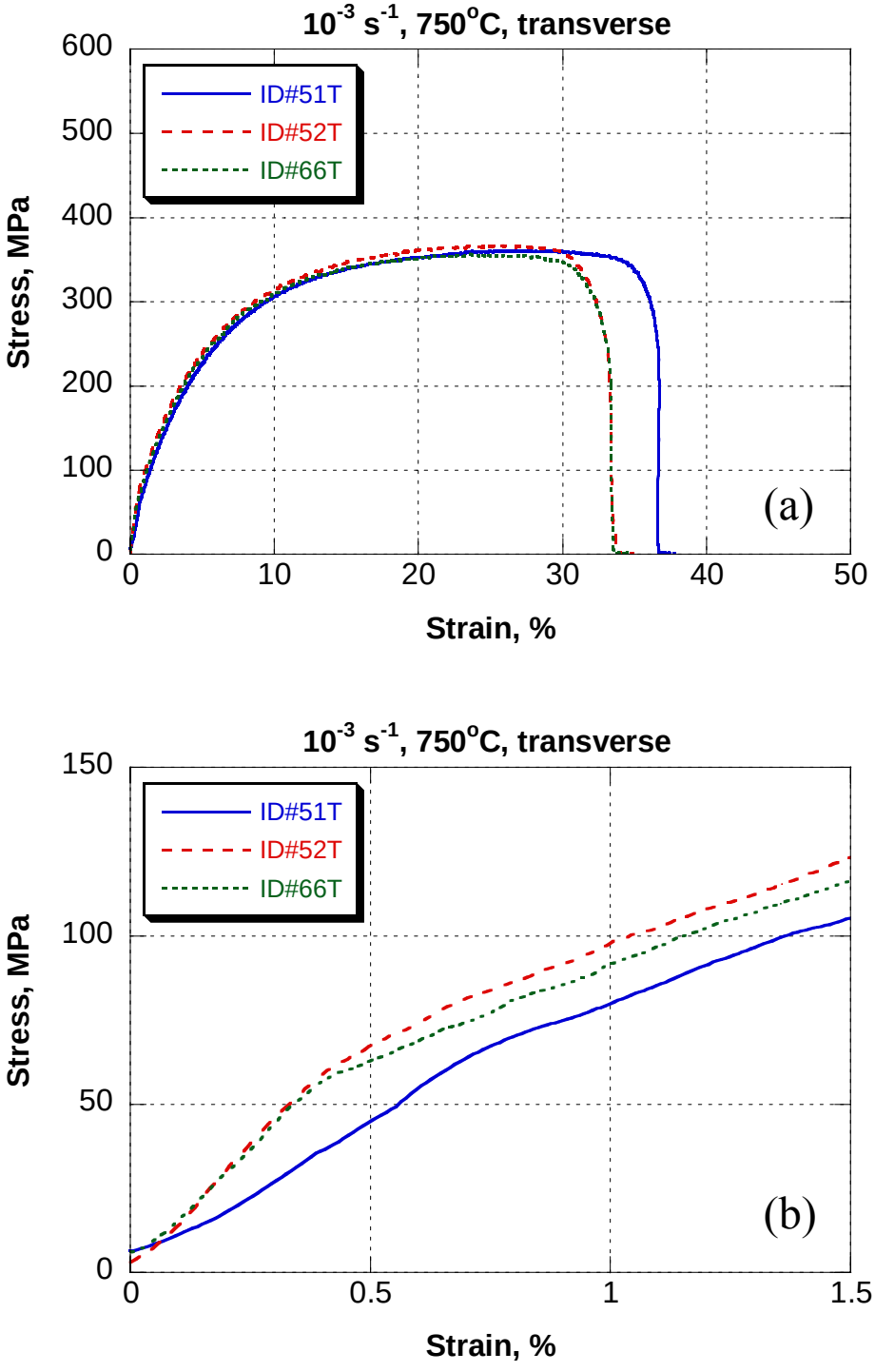

Fig. 18. Stress-strain curves at 10^{-3} s^{-1} and 750°C, transverse specimen orientation, (a) full curves, (b) yield region.

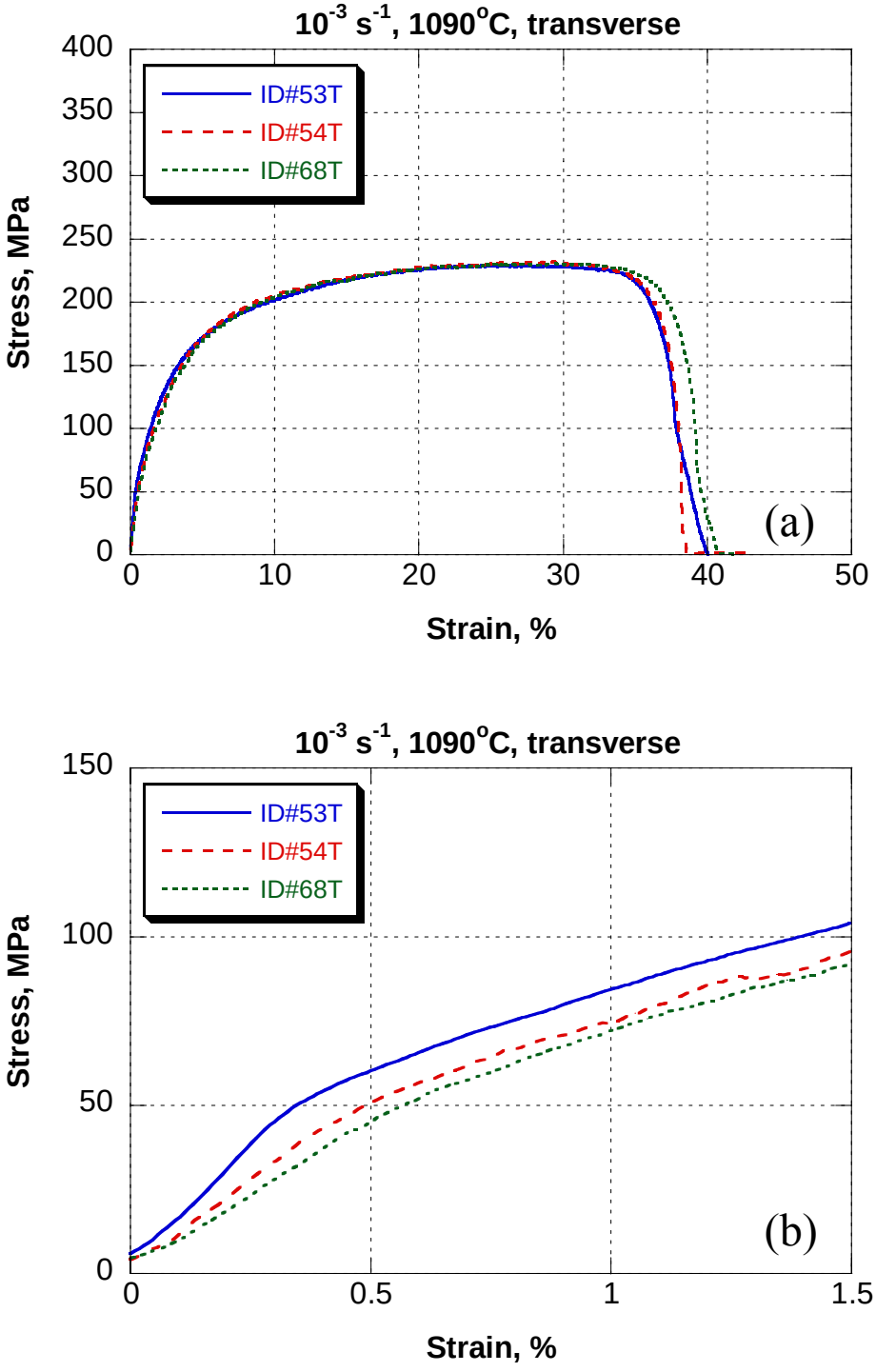

Fig. 19. Stress-strain curves at 10^{-3} s^{-1} and 1090°C, transverse specimen orientation, (a) full curves, (b) yield region.

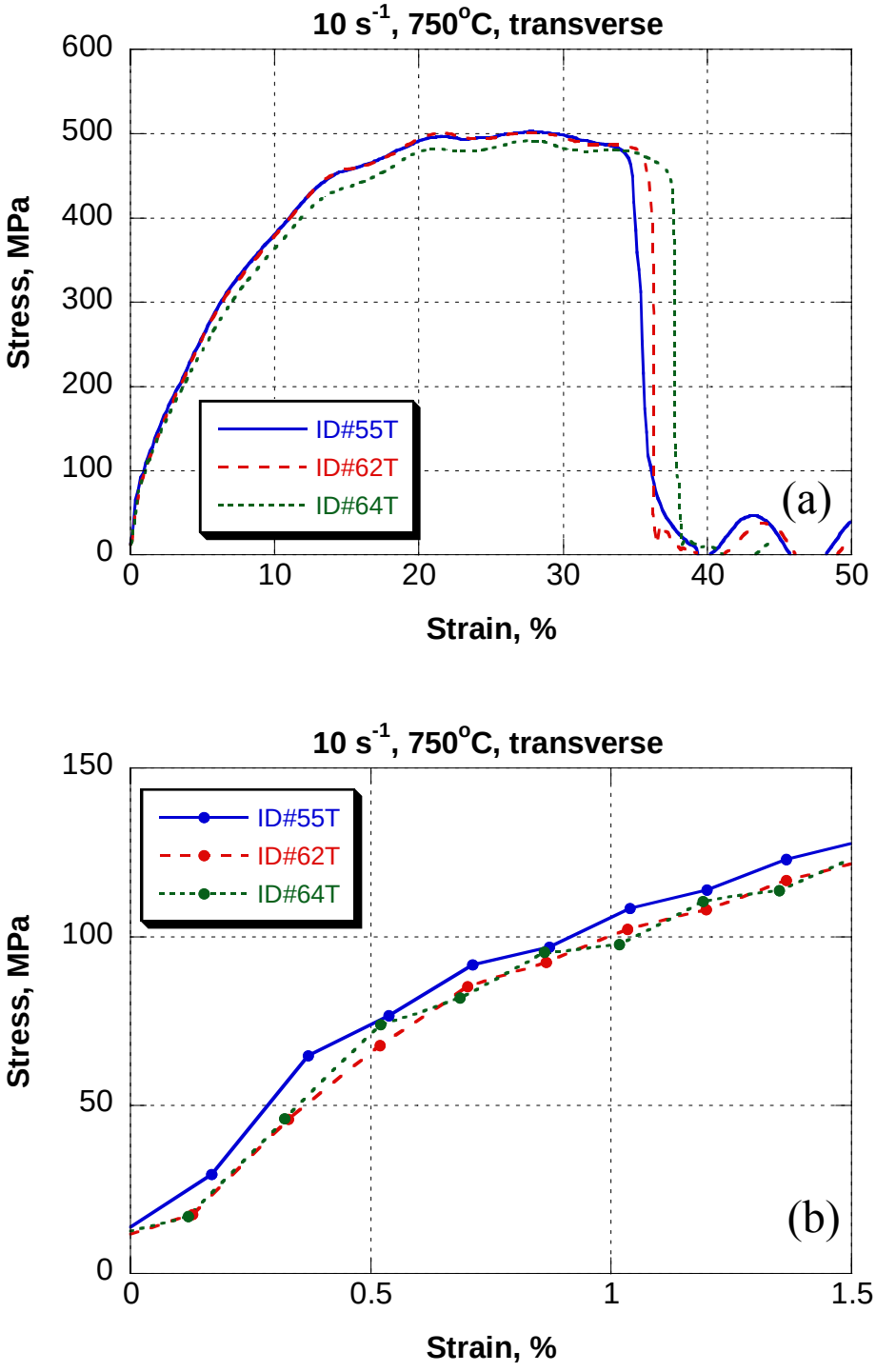

Fig. 20. Stress-strain curves at 10 s^{-1} and 750°C, transverse specimen orientation, (a) full curves, (b) yield region.

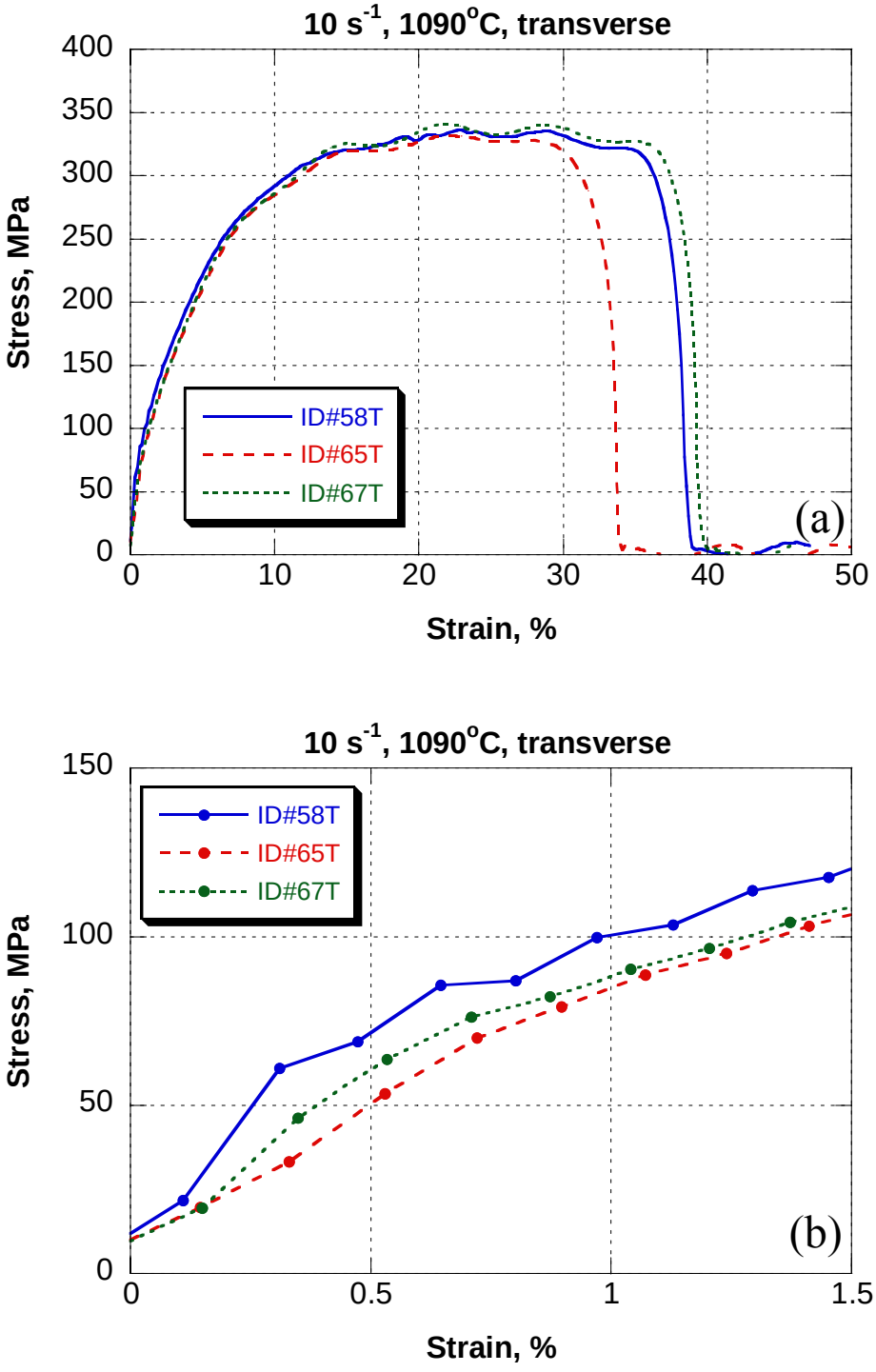

Fig. 21. Stress-strain curves at 10 s^{-1} and 1090°C, transverse specimen orientation, (a) full curves, (b) yield region.

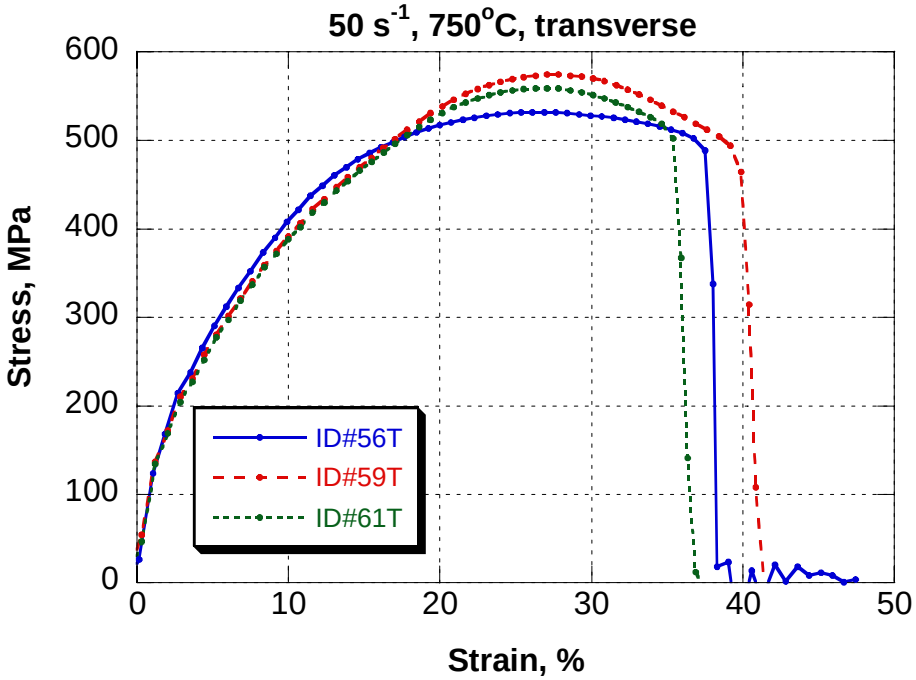

Fig. 22. Stress-strain curves at 50 s^{-1} and 750°C, transverse specimen orientation.

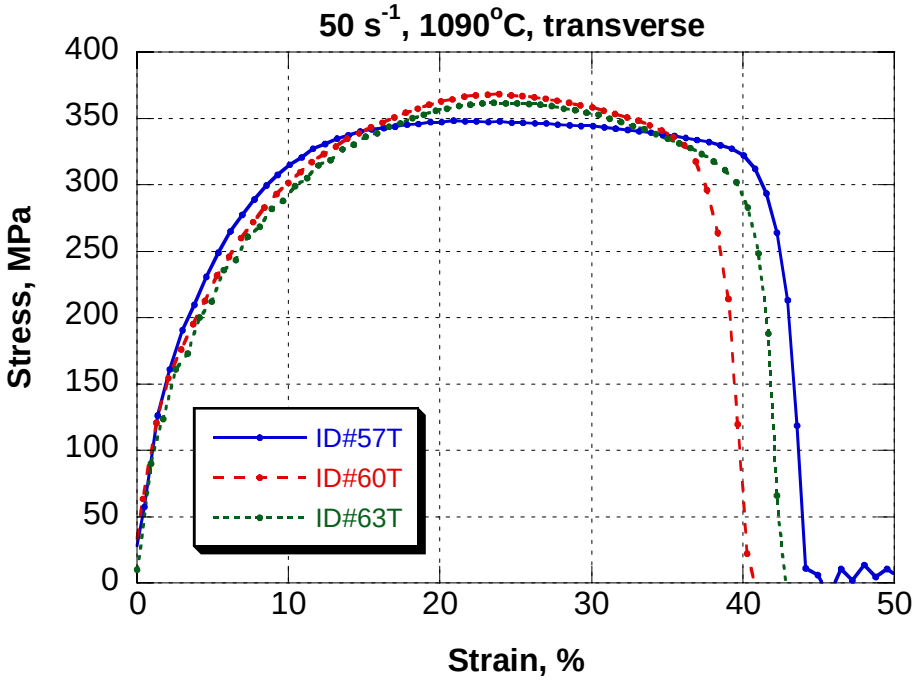

Fig. 23. Stress-strain curves at 50 s^{-1} and 1090°C, transverse specimen orientation.

YIELD STRESS, ULTIMATE TENSILE STRESS, FRACTURE STRAIN, REDUCTION IN AREA

The 0.2% yield stresses (YS), ultimate tensile stresses (UTS) and fracture strains (elongations to fracture) were evaluated from the curves in Figs. 3-23. These values as well as the reduction in area (RA) values are summarized in Tables IV and V. Table VI compares the average values for nominally identical tests, for longitudinal as well as transverse specimens. The corresponding plots are shown in Figs. 24-27. Typical standard deviations, in % of the average value, were 5% for the YS, 2% for the UTS, 6% for the ductility, and 6% for the RA. Figure 24 shows that the yield stress decreases as the temperature increases, and that higher strain rates result in higher yield stresses, i.e., the material is strain rate sensitive. The yield stress values at 10^{-3} s^{-1} tend to be slightly lower and less scattered than the corresponding DOP-26 values shown in George et al. [10]. The strain rate sensitivity of DOP-26 is clearly illustrated for the UTS values in Fig. 25. As compared to George et al. [10], the room temperature UTS is higher, whereas the UTS values at >600°C tend to be lower. The fracture strain increases substantially when the test temperature is increased from ambient to 600°C (Fig. 26). As the temperature is increased further, one observes a slight trend towards increased fracture strains. Within the scatter of the data, the fracture strains at 600°C and above do not appear to depend on the strain rate. However, this does not preclude a reduction in the fracture strain for strain rates well in excess of 50 s^{-1}. The reduction in area is more sensitive to the temperature and strain rate than the fracture strain. For example, while the RA at 900°C and 10^{-3} s^{-1} is close to 100%, an increase in the strain rate to 10 or 50 s^{-1} reduces its value by approximately 50% (Fig. 27). Within the window of temperature and strain rates examined, the mechanical properties do not appear to be sensitive to the testing orientation, although there may be a trend towards lower ductility for the transverse specimens.

Heestand et al. [12] previously examined the effect of the testing orientation on the ductility at 925°C (Table VII). The strain rate, 0.67 s^{-1}, was intermediate between the values of 1×10^{-3} and 10 s^{-1} in the present report. Heestand et al.'s material was not recrystallized – it was only stress-relieved by annealing for 1 hour at 1025°C. Not surprisingly, the UTS values, approximately 700 MPa, were higher than the approximately 400 MPa in the present report. Similarly, the stress-relieved material is much less ductile than the fully recrystallized material.

In disagreement with the present results, Heestand et al.'s data indicates a significantly lower ductility for the transverse orientation as compared to the longitudinal one. One reason for this difference may be the fact that the specimens in the present work were fully recrystallized by annealing for 1 hour at 1375°C. The recrystallization may have alleviated the anisotropy, as compared to the stress-relieved compositions. However, it cannot be ruled out that anisotropy might be observed even in fully recrystallized material at strain rates well above 50 s^{-1}.

Table IV. Longitudinal DOP-26 iridium (Sheet identification K3-14) at different strain rates and temperatures (T): 0.2% yield stress (YS), ultimate tensile stress (UTS), fracture strain (elongation to fracture), and reduction in area (RA)

ID#	Strain Rate, s^{-1}	T, °C	0.2% YS, MPa	UTS, MPa	Fracture strain, %	RA, %
1	1×10^{-3}	25	119	690	8.9	5.9
32	1×10^{-3}	25	126	700	8.9	11.2
43	1×10^{-3}	25	127	769	10.5	7.3
2	1×10^{-3}	600	92	436	32.6	59.8
19	1×10^{-3}	600	78	441	28.6	49.7
33	1×10^{-3}	600	83	438	30.3	53.8
20	1×10^{-3}	750	83	342	33.2	98.5
35	1×10^{-3}	750	77	341	32.2	88.8
4	1×10^{-3}	900	75	289	35.1	91.1
21	1×10^{-3}	900	88	282	34.9	97.2
36	1×10^{-3}	900	77	274	36.8	93.6
5	1×10^{-3}	1090	57	203	40.0	99.2
37	1×10^{-3}	1090	62	206	39.1	95.3
45	1×10^{-3}	1090	70	199	39.0	97.2
6	10	25	133	782	9.7	10.2
23	10	25	133	772	10.0	9.8
38	10	25	137	838	11.4	10.2
7	10	600	90	565	30.8	43.1
24	10	600	96	590	32.2	42.6
39	10	600	109	612	33.4	36.6
8	10	750	96	496	34.6	54.2
25	10	750	92	486	30.0	55.2
40	10	750	96	485	33.9	53.7
9	10	900	84	400	31.2	57.9
26	10	900	81	390	24.9	53.8
41	10	900	84	397	31.2	65.0
11	10	1090	76	312	37.1	97.1
27	10	1090	79	310	37.0	88.7
42	10	1090	83	317	33.9	95.1
12	50	25		765	9.6	9.2
28	50	25		793	9.9	9.0
44	50	25		753	8.9	8.9
13	50	600		645	33.9	38.4
29	50	600		650	34.9	38.7
50	50	600		666	33.1	44.2
14	50	750		526	38.7	49.2
30	50	750		539	36.3	49.4
48	50	750		543	36.6	51.3
15	50	900		433	32.9	58.4
17	50	900		438	32.2	46.8
47	50	900		430	32.9	59.0
16	50	1090		347	44.5	99.3
46	50	1090		351	35.5	98.4
49	50	1090		347	34.7	98.5

Table V. Transverse DOP-26 iridium (blank identifications GR9-1 #4; GR9-2 #1, #4, #5, #6, #7) at different strain rates and temperatures (T): 0.2% yield stress (YS), ultimate tensile stress (UTS), fracture strain (elongation to fracture), and reduction in area (RA)

ID#	Strain rate, s^{-1}	T, °C	0.2% YS, MPa	UTS, MPa	Fracture strain, %	RA, %
51T	0.001	750	92	361	33.1	79.7
52T	0.001	750	84	367	30.5	85.2
66T	0.001	750	75	357	30.5	86.1
53T	0.001	1090	68	229	35.4	94.8
54T	0.001	1090	67	232	35.1	98.8
68T	0.001	1090	70	231	35.8	96.1
55T	10	750	92	503	32.7	44.9
62T	10	750	92	498	33.3	54.1
64T	10	750	95	485	35.0	48.2
58T	10	1090	83	333	35.8	99.1
65T	10	1090	89	329	29.8	100.0
67T	10	1090	80	337	36.1	97.2
56T	50	750		532	34.9	45.0
59T	50	750		575	35.7	48.5
61T	50	750		559	32.6	46.6
57T	50	1090		348	40.0	98.8
60T	50	1090		368	35.4	96.4
63T	50	1090		362	38.1	99.8

Table VI. Averaged mechanical properties for longitudinal and transverse DOP-26 iridium alloy

Strain rate, s^{-1}	T, °C	YS, MPa	YS, MPa	UTS, MPa	UTS, MPa	Fracture strain, %	Fracture strain, %	RA, %	RA, %
		Long.	*Trans.*	*Long.*	*Trans.*	*Long.*	*Trans.*	*Long.*	*Trans.*
1×10^{-3}	25	124		720		9.4		8.1	
1×10^{-3}	600	84		438		30.5		54.4	
1×10^{-3}	750	80	84	342	362	32.7	31.4	93.7	83.7
1×10^{-3}	900	80		282		35.6		94.0	
1×10^{-3}	1090	63	68	203	231	39.4	35.4	97.2	96.6
10	25	134		797		10.4		10.1	
10	600	98		589		32.1		40.8	
10	750	95	93	489	495	32.8	33.7	54.4	49.1
10	900	83		396		29.1		58.9	
10	1090	79	84	313	333	36.0	33.9	93.6	98.8
50	25			770		9.5		9.0	
50	600			654		34.0		40.4	
50	750			536	555	37.2	34.4	50.0	46.7
50	900			434		32.7		54.7	
50	1090			348	359	38.2	37.8	98.7	98.3

Table VII. Heestand et al. tensile data [12] for stress-relieved (1h/1025°C) DOP-26 iridium alloy (B2-7 sheet) tested at 925°C and 6.7×10^{-1} s^{-1}

Orientation	UTS, MPa	Elongation*
longitudinal	745	10.6
longitudinal	645	13.6
transverse	628	8.1
Transverse	692	9.6

*Ref. [12] does not provide details on the way in which the elongation to fracture was obtained.

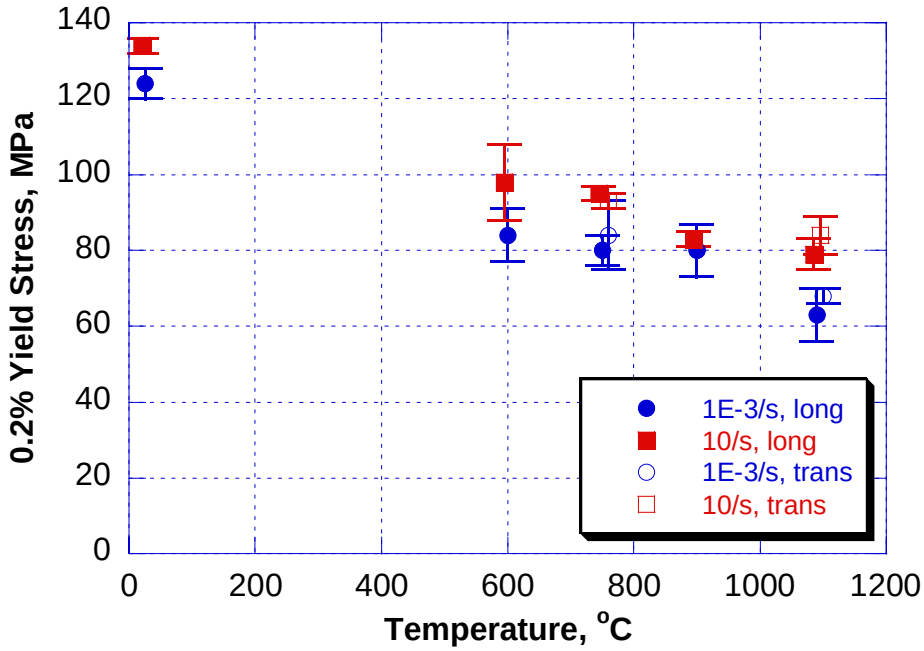

Fig. 24. Plot of yield stress vs. temperature for longitudinal and transverse orientations at different strain rates. The temperatures are shifted by small amounts in order to separate the standard deviation error bars.

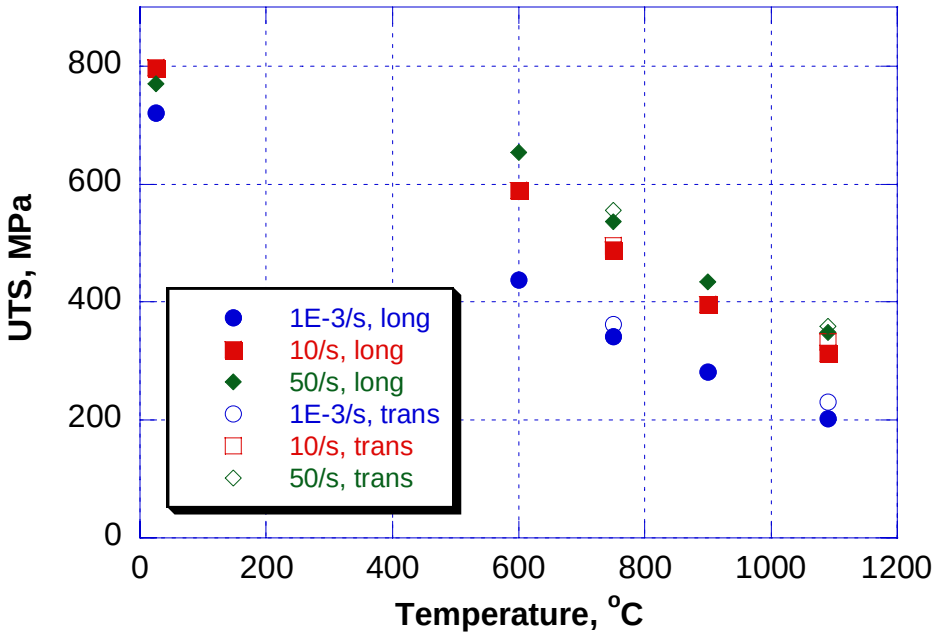

Fig. 25. Plot of ultimate tensile stress vs. temperature for longitudinal and transverse orientations at different strain rates.

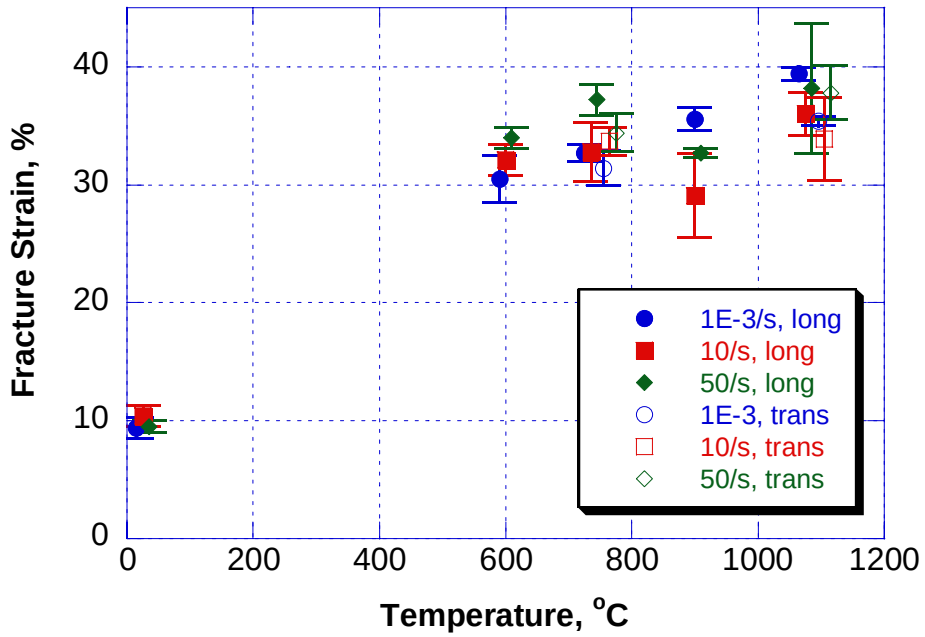

Fig. 26. Plot of fracture strain vs. temperature for longitudinal and transverse orientations at different strain rates. The temperatures are shifted by small amounts in order to separate the standard deviation error bars.

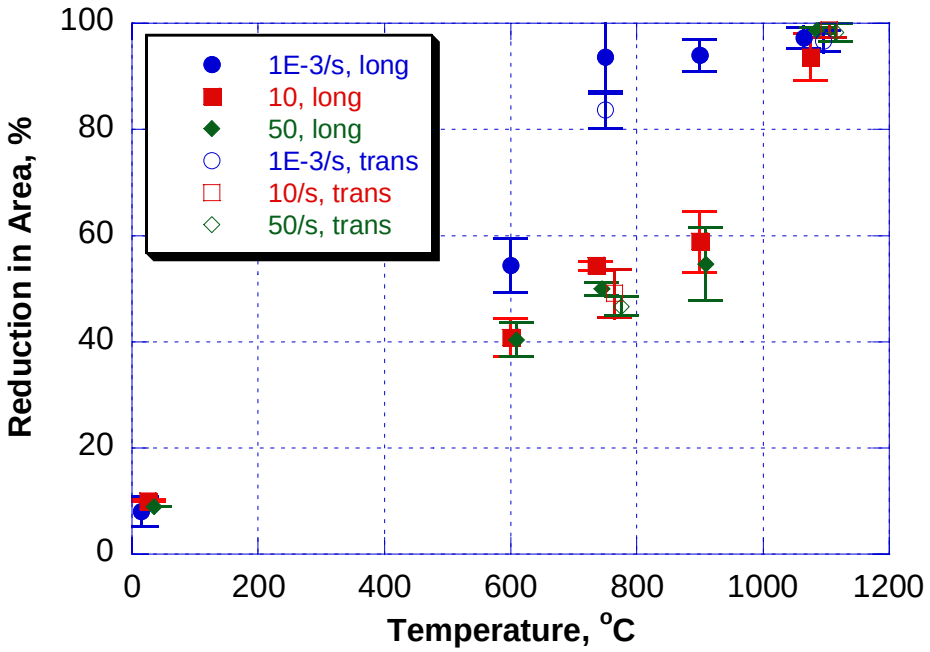

Fig. 27. Plot of reduction in area vs. temperature for longitudinal and transverse orientations at different strain rates. The temperatures are shifted by small amounts in order to separate the standard deviation error bars.

NON-UNIFORMITY OF DEFORMATION

As long as adequate work-hardening occurs during a tensile test, the deformation in the gage section is uniform since the work-hardening counteracts the development of above-average local strains. At elevated temperatures, the work hardening rate decreases and non-uniform deformation is more likely to occur. Assuming that the mechanical properties in each specimen are homogeneous, any non-uniformity in the strain is due to non-uniformities in the gage cross section as well as temperature gradients along the gage. The exact specimen contours were not determined in this work, only the minimum and maximum widths in the center and the radii at the ends of the gage sections. Also, the temperature gradient was not measured rigorously – the only requirement was for the temperatures of the two thermocouples attached to the gage (with a separation about 5 mm) not to differ by more than 20°C. Tables VIII and IX tabulate the local strains evaluated from the spacing of adjacent indents for longitudinal and transverse specimens. Consistent with the high work hardening capacity, the strains in the gage sections are quite uniform at room temperature. At elevated temperatures, however, significant strain gradients develop because the work hardening rate is essentially zero for a large fraction of the test. This is illustrated in Figs. 28 and 29, which compare the local indent strains for the longitudinal specimens tested between 600 and 1090°C at strain rates of 1×10^{-3} and 50 s^{-1}, respectively. A comparison of the two figures shows clearly that the scatter is particularly high at the lower strain rate, for which the lowest amount of work hardening occurs.

Table VIII. Local strains determined from the change in spacing of indents 1 through 7 for longitudinal DOP-26 specimens

ID#	Strain rate, 1/s	T, C	1-2, %	2-3, %	3-4, %	4-5, %	5-6, %	6-7, %	Indent fracture strain, %
1	1×10^{-3}	25	8.8	8.4	8.7	8.5	8.7	8.6	8.6
32	1×10^{-3}	25	8.5	8.9	8.9	9.7	8.7	8.8	9.0
43	1×10^{-3}	25	9.2	10.6	10.8	9.8	9.9	9.9	10.0
2	1×10^{-3}	600	44.4	56.2		29.2	23.7	20.2	34.7
19	1×10^{-3}	600		36.6	28.9	23.6	21.2	18.5	25.8
33	1×10^{-3}	600		35.5	31.5	29.7	24.1	21.8	28.5
20	1×10^{-3}	750	45		39.5	27.3	23.7	18.9	30.8
35	1×10^{-3}	750	29.9		45.8	34	28.9	23.6	32.4
4	1×10^{-3}	900		46.1	39.2	30	27.5	24.4	33.5
21	1×10^{-3}	900	53.4		39.7	32.7	26	22.2	34.8
36	1×10^{-3}	900		51	38.1	39.6	38.2	26.9	38.8
5	1×10^{-3}	1090	34.7	42.1		44.8	40.1	34	39.1
37	1×10^{-3}	1090		58.2	46.9	34.2	28.4	23.3	38.2
45	1×10^{-3}	1090	56.5		48.4	35.7	34.6	28.6	40.8
6	10	25	10.1		10.2	10	9.9	10.1	10.1
23	10	25	9.1	10.1	9.2	9.5	9.4	9.0	9.4
38	10	25	11.1	11.1	12.9	11.1	11.3	10.6	11.4
7	10	600	26.8	30.4	33.3	37.1	37.9		33.1
24	10	600	28.6	33.7	38.9		34.6	26.9	32.5
39	10	600	27.1		43	40	34.3	28.8	34.6
8	10	750	37.4	49.5			36.3	30.2	38.3
25	10	750		32.4	27.6	27.8	25.9	23	27.3
40	10	750	35.5		42.9	40.4	31.6	28.7	35.8
9	10	900	29	32.8		33.1	30.9	26.9	30.5
26	10	900		32.9	26.8	25.5	22.2	21.3	25.7
41	10	900	35.4	47.6		30.7	25.7	21.7	32.2
11	10	1090	21.8	29.1	36.5	41	48.3		35.4
27	10	1090	36.8	45.8	41.7		43.5	32.5	40.1
42	10	1090	36.8		60.8	32.2	26	21.4	35.5
12	50	25	9.6		9.4	9.9	9.4	9.1	9.5
28	50	25	10	10.6	10.2	10.4	10.5	10.3	10.3
44	50	25	9.5	9.4	9.7	9.0	8.7	9.9	9.4
13	50	600	26.9	31.2	36.3	39.2			33.4
29	50	600	31.2	37.9		38.2	29.7	28.6	33.1
50	50	600	32.6		41.6	35.8	32.2	30.4	34.5
14	50	750	30.6	33.9	43.5	39.3	43.6		38.2
17	50	750	28.5	31.1	32.3	31.2		37.5	32.1
48	50	750	34.3	39.4	49		38.4	31.8	38.6
15	50	900	25.4	28.3	30.5			37.8	30.5
30	50	900	33.9			41.8	34.3	27.7	34.4
47	50	900	35.6	42.5		34.2	29.9	25.7	33.6
16	50	1090	51.6			56.2	41.4	35.3	46.1
46	50	1090	32.8	37.9	40.1			28.5	34.8
49	50	1090	32.3			36.9	29.5	25.8	31.1

Table IX. Local strains determined from the change in spacing of indents 1 through 7 for transverse DOP-26 specimens

ID#	Strain rate, s^{-1}	T, C	1-2, %	2-3, %	3-4, %	4-5, %	5-6, %	6-7, %	Indent fracture strain, %
51T	1×10^{-3}	750	21.2	24	32.9	39.9	49.2		33.4
52T	1×10^{-3}	750	24.6	27.3	26.8	31	37.8		29.5
66T	1×10^{-3}	750	20.9	23.2	26.3	30.4	35.9		27.3
53T	1×10^{-3}	1090	24.4	27.5	34		46.6	49.1	36.3
54T	1×10^{-3}	1090	28	30.1	30.7	31.6			30.1
68T	1×10^{-3}	1090	20.3	29.4	32.3	40.4	39.9	50.4	35.5
55T	10	750	26.3	29.1	33.4	36		31.2	31.2
62T	10	750	26.4	35.5	40.1	38.9	39.1		36.0
64T	10	750	29	33.4	38.3		37	31.4	33.8
58T	10	1090	26.4	30.7	39.3	51.1		43.8	38.3
65T	10	1090	21.5	27.4	26.7	28.2	33.2		27.4
67T	10	1090	31.6	39.9		42.1	43.4	36.2	38.6
56T	50	750	32.5	33	31.5	36	44.6		35.5
59T	50	750	28.4	30.5	36.8	51.8		43	38.1
61T	50	750	25.6	30.5	33.4	35.9	41.5		33.4
57T	50	1090	34.8		42.3	37.9	39.9	50.7	41.1
60T	50	1090	24.4	29.1	38.4	40.5	39.5		34.4
63T	50	1090	24.6	30.9	38.2		43.7	61.1	39.7

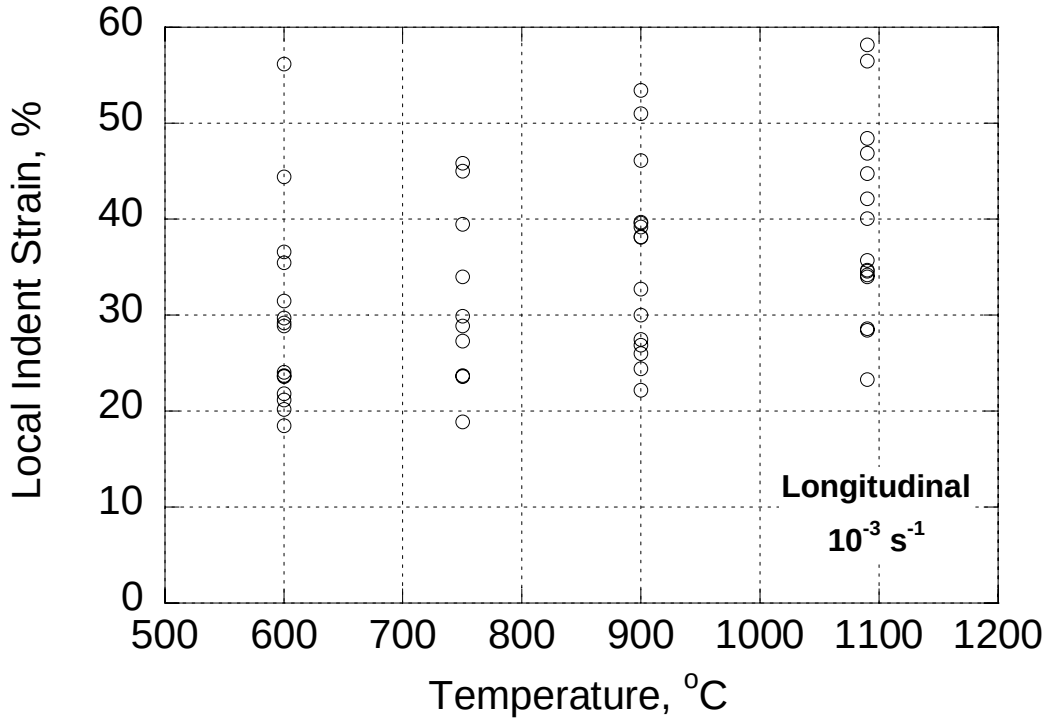

Fig. 28. Local indent fracture strains for longitudinal DOP-26 specimens tested at 1×10^{-3} s^{-1}.

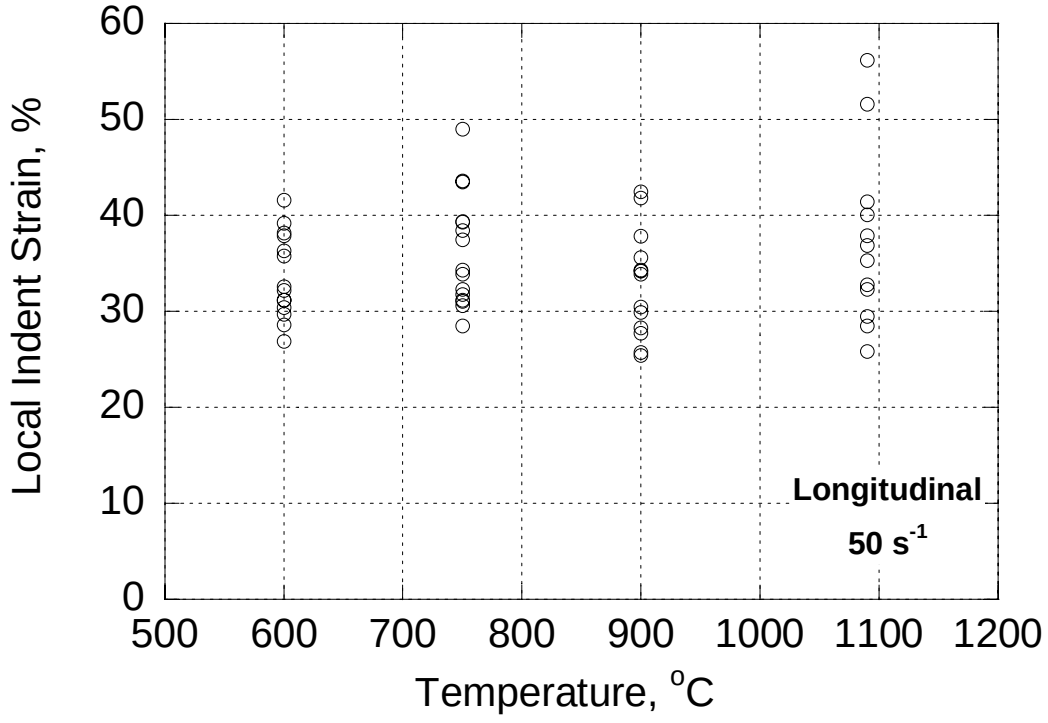

Fig. 29. Local indent fracture strains for longitudinal DOP-26 specimens tested at 50 s^{-1}.

SUGGESTIONS FOR FURTHER WORK

While the mechanical property data obtained in this work adds to the data base for DOP-26, further improvements in the testing procedure as well as tests at significantly higher strain rates are desirable. A list of suggestions for further work follows:

1. Proof-of-principle tests should be performed to determine whether a flat area of contact between the specimen and grip will minimize the plastic deformation observed in the head section at stresses below the macroscopic yield stress.

2. At strain rates above 10 s^{-1}, data acquisition rates much higher than the 5 kHz used in the present work are required.

3. In order to minimize the temperature gradients along the gage length it would be desirable to permanently attach at least three thermocouples to a Pt strip, with the spacing of the two outer thermocouples being 10 mm. The Pt strip instrumented in this way should then be wire-wrapped to the gage length of the specimens. With three or more thermocouples it will be easier to minimize any temperature gradients by the susceptor design and position.

4. The measurements of the indent fracture strains show significant scatter from specimen to specimen. If the number of indents would be increased above the present value of 7, the accuracy of the strain measurements would be improved. It may also be worth considering other ways of strain measurement. For example, modern inspection equipment makes it easy to automatically measure the detailed shape of a specimen before and after testing in order to calculate the local strains at very small intervals along the gage length.

5. The maximum strain rate employed in the present work, 50 s^{-1}, may not be fast enough to convincingly demonstrate the effect of strain rate on ductility and testing direction (transverse vs. longitudinal). However, at a strain rate of 50 s^{-1} ringing of the load cell does already become a problem. Extending the experiments to strain rates of 500 or 1000 s^{-1} at elevated temperatures will likely involve a significant research effort.

SUMMARY AND CONCLUSIONS

DOP-26 specimens in the recrystallized condition (vacuum anneal of 1 hour at 1375°C) were tested in tension in orientations parallel and perpendicular to the rolling direction of the sheet from which they were fabricated. The tests were performed at temperatures ranging from room temperature to 1090°C and strain rates ranging from 1×10^{-3} to 50 s^{-1}. Room temperature testing was performed in air, while testing at elevated temperatures was performed in a vacuum better than 1×10^{-4} Torr. The yield stress (YS) and the ultimate tensile stress (UTS) values decreased with increasing temperature and decreasing strain rate. Between 600 and 1090°C, the ductility (elongation to fracture) showed a slight increase with increasing temperature, whereas, within the scatter of the data, the ductility did not depend on the strain rate. The reduction in area (RA), on the other hand, decreased with increasing strain rate. The YS and UTS values did not differ significantly for the longitudinal and transverse specimens. The ductility and RA values of the transverse specimens were marginally lower than those of the longitudinal specimens.

While the results of this report add significantly to the data base on the mechanical properties of DOP-26, it would be desirable to improve and extend the data. An improved specimen-grip design to minimize plastic deformation during seating of the specimens prior to yielding, improved control of temperature gradients along the gage length, and increased data collection rates are desirable. Strain rates between 50 to 5000 s^{-1} need to be examined in order to fully characterize the strain rate sensitivity of the mechanical properties of DOP-26. Such tests will require special precautions in order to minimize ringing of the load cell, and their successful implementation will likely require a significant research effort.

REFERENCES

1. E. P. George and C. T. Liu, *Micro- and Macro-Alloying of Ir-Base Alloys*, in Iridium (eds. E. K. Ohriner, R. D. Lanam, P. Panfilov, and H. Harada), The Minerals, Metals and Materials Society, Warrendale, PA, 2000, pp. 3-14.

2. C. T. Liu and H. Inouye, *Study of Iridium and Iridium-Tungsten Alloys for Space Radioisotopic Heat Sources*, Report ORNL-5240, Oak Ridge National Laboratory, Oak Ridge, Tennessee, December 1976.

3. C. T. Liu and H. Inouye, *Development and Characterization of an Improved Ir-0.3% W Alloy for Space Radioisotopic Heat Sources*, Report ORNL-5290, Oak Ridge National Laboratory, Oak Ridge, Tennessee, October 1977.

4. C. T. Liu, H. Inouye, and A. C. Schaffhauser, *Metallurgical and Mechanical Properties of Thorium-Doped Ir-0.3% W Alloys*, Report ORNL-5616, Oak Ridge National Laboratory, Oak Ridge, Tennessee, April 1980.

5. C. T. Liu, H. Inouye, and A. C. Schaffhauser, Metall. Trans. A, 12A (1981) 993-1002.

6. H. Inouye and C. T. Liu, *Iridium-Hafnium Alloy*, U.S. Patent 3,918,965, November 11, 1975.

7. C. L. White, R. E. Clausing, and L. Heatherly, Metall. Trans. A, 10A (1979) 683-691.

8. T. G. George and M. F. Stevens, JOM, 40 (Oct 1988) 32-35.

9. A. N. Gubbi, E. P. George, E. K. Ohriner, and R. H. Zee, Metall. Mater. Trans. A, 28A (1997) 2049-2057.

10. E. P. George, C. G. McKamey, E. K. Ohriner, and E. H. Lee, Mater. Sci. Eng. A319-321 (2001) 466-470.

11. G. B. Ulrich, *Heat-Resistant Materials*, edited by K. Natesan and D. J. Tillack, ASM International, Materials Park, Ohio, 1991, pp. 187-195.

12. R. L. Heestand, E. K. Ohriner, and T. K. Roche, *Advances in Iridium Alloy Processing in 1987*, Report ORNL/TM-10852, Oak Ridge National Laboratory, August 1988.

INTERNAL DISTRIBUTION

1. C. A. Carmichael
2. E. P. George
3-4. J. F. King
5. E. K. Ohriner
6. R. G. Miller
7-9. J. H. Schneibel
10. G. B. Ulrich
11. S. J. Zinkle
12. ORNL Technical Information Office (RC)

EXTERNAL DISTRIBUTION

13. Robert T. Carpenter, Orbital Sciences Corporation 20030 Century Blvd., Suite 102, Germantown, MD 20874
14. John Dowicki, Office of Radioisotope Power Systems, NE-34/GTN, U. S. Department of Energy, 1000 Independence Avenue SW, Washington, DC 20585-1290
15. Stephen G. Johnson, Idaho National Laboratory, P. O. Box 1622, MS-6122, Idaho Falls, ID 83415
16. Office of Scientific and Technical Information (PDF file to ORNL Releasing Official, R. P. Migun)
17. Emil Skraek, Orbital Sciences Corporation, 2003 Century Blvd., Suite 102, Germantown, MD 20874
18. Craig E. Van Pelt, Los Alamos National Laboratory, P. O. Box 1633, Los Alamos, NM 87545
19. Robert L. Wiley, Office of Radioisotope Power Systems, NE-34/GTN, U. S. Department of Energy, 1000 Independence Avenue SW, Washington, DC 20585-1290